RECONFIGURABLE LEAKY WAVE ANTENNA WITH TUNABLE IMPEDANCE SURFACES

by

Ulysses Ungos

A thesis submitted to the faculty of
The University of North Carolina at Charlotte
in partial fulfillment of the requirements
for the degree of Master of Science in
Electrical Engineering

Charlotte

2022

Approved by:

_____
Dr. Mario J. Mencagli, Ph.D.

_____
Dr. Abasifreke Ebong, Ph.D.

_____
Dr. Kathryn L. Smith, Ph.D.

ABSTRACT

ULYSSES UNGOS. Reconfigurable Leaky Wave Antenna with tunable impedance Surfaces. (Under the direction of DR. MARIO J. MENCAGLI, PH.D.)

This thesis describes a novel design of a reconfigurable modulated metasurface (MTS) antenna. Currently, antennas are designed and created with exact parameters to meet specific demands. The demands can change instantly in the ever-changing world of space communication or the Internet of Things. The proposed antenna comprises a modulated metasurface and a ground plane connected with two Piezoelectric actuators. The actuators provide the means for changing the distance between the metasurface and the ground plane to adjust the direction in which the antenna is radiating. A single unit cell is studied and used to configure the modulation in the metasurface. This paper also discusses the preliminary design considerations for the ability of the antenna to beam steer as well as techniques for optimization. Full-wave simulations have verified the antenna's performance in hopes of future fabrication and testing for further verification.

This thesis also discusses the laws and properties that define the behavior of electromagnetic waves as well as the mediums they travel through. The history of metamaterials and the research for metasurfaces currently in use are covered. Metasurfaces offer advantages in terms of size, weight, cost, and scalability compared to traditional optical systems for the same functionality in various technology fields.

DEDICATION

In memory of Joel and Bryce.

And to Ava, Jayce, Chloe, Olivia, and any other nieces or nephews that are born after. Math and science is cool, I hope you find some joy in them as much as I have.

ACKNOWLEDGEMENTS

I want to thank Dr. Mario Junior Mencagli for your guidance and advising. I am genuinely grateful for the conversations you've shared with me as well as your insight. You brought me into the field, with Fields, and I can not thank you enough for everything else along the way.

I would also like to share my appreciation with my committee members, Dr. Abasifreke Ebong and Dr. Kathryn Smith. Time spent in class and your thoughts and perspective about continuing education really had an impact on me. Special acknowledgment to Kristy for your unwavering supply of help and support.

I would also want to recognize my friends and my family members. If I were to put down the names of you all and talk about the support and care you provided for me I would probably have two more chapters. So I will show this appreciation to you every moment we get to share together. Thank you all so much.

TABLE OF CONTENTS

LIST OF TABLES

LIST OF FIGURES

LIST OF ABBREVIATIONS

ϵ A symbol for permitivity

μ A symbol for permeability

μm An abbreviation for micrometers

HFSS An acronym and shorthand referring to Ansys high-frequency structure simulator

IBC An acronym impedance boundary conditions

MTM An acronym for metamaterial

MTS An abbreviation for metasurface

PEC An acronym for Perfect Electric Conductor

RF An acronym for Radio Frequency

TE An acronym for Transverse Electric

TM An acronym for Transverse Magnetic

CHAPTER 1: BACKGROUND

1.1 Introduction

Metamaterials (MTMs) are synthetic materials structured at a subwavelength scale. They are constructed at the microscopic or nanoscopic level with periodically arranged patterns with gradual changes in a dielectric environment. The result is a medium that interacts with waves coming from light or other forms of energy in ways not occurring naturally. These patterns, along with the material's composition, can be used to control and manipulate light or energy in different ways, such as changing the beam propagation direction, polarization change, shaping the wavefront, or partitioning the energy.

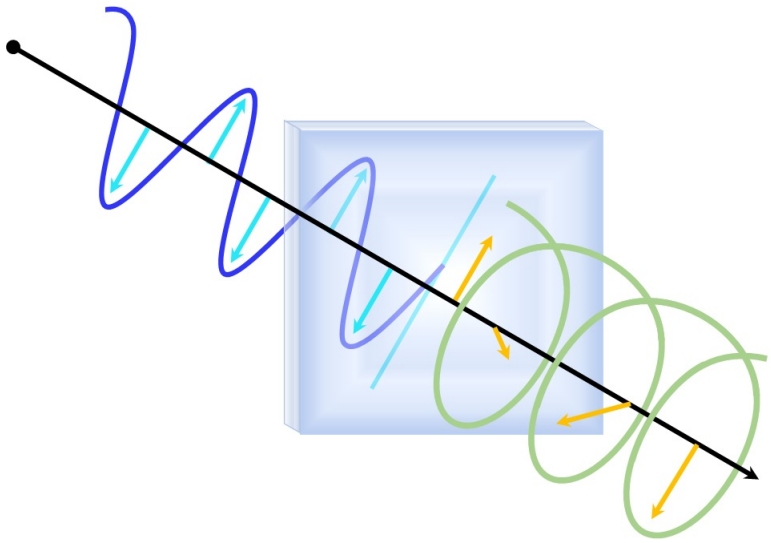

Figure 1.1: Metamaterials and metasurfaces can be used to control light or energy in different ways. One application is changing the polarization of a propagating wave. In this example, a linearly polarized wave is traveling. When it goes through the metasurface, it changes from linear to circular polarization.

The two-dimensional counterpart of metamaterials is the metasurface (MTSs).

Similarly, metasurfaces are made of a thin layer of material that can be used to control the phase and amplitude of the electromagnetic waves that pass through it. One of the most significant advantages metasurfaces offer is their planar structure. They occupy less space and demonstrate lower losses compared to traditional metamaterial structures. This property makes them ideal for today's technology which is getting smaller and more compact. From its humble beginnings, the implementation of metasurfaces can and is being used in various applications such as in space communications, with satellites and radars, in electromagnetic devices on the surfaces of vehicles and aircraft, and in the sensors and systems of various applications relating to the Internet of Things. The field of metasurface research is rapidly evolving in the ever-growing world of technology, and new applications and variants are discovered every year.

1.2 History of Metamaterials

In the early days, metamaterials were nothing more than a theoretical curiosity. In the past few decades, they have become one of the most promising areas of research in both physics and engineering. The idea of MTMs can be traced back to V.G. Veselago when he proposed unnatural phenomena such as an inversion of the Doppler shift (Fig. 1.2a), an inverse effect of Cerenkov radiation (Fig. 1.2b), and 'negative refraction' (Fig. 1.2c). For these situations to occur, he suggested a substance with both negative permeability, μ, and permittivity, ε, co-occurring at the same frequency. Veselago explored this material and its properties using the Maxwell equations and the constitutive relations of a propagating electromagnetic wave's electric and magnetic fields. He stated that "when $\varepsilon > 0$ and $\mu > 0$, the resulting direction vectors of the wave formed a classic right-handed triplet, and when $\varepsilon < 0$ and $\mu < 0$, the vectors were part of a left-handed set [6]." This was the first step in understanding the physics behind his theorized phenomena, ultimately leading to the expression 'left-handed material.'

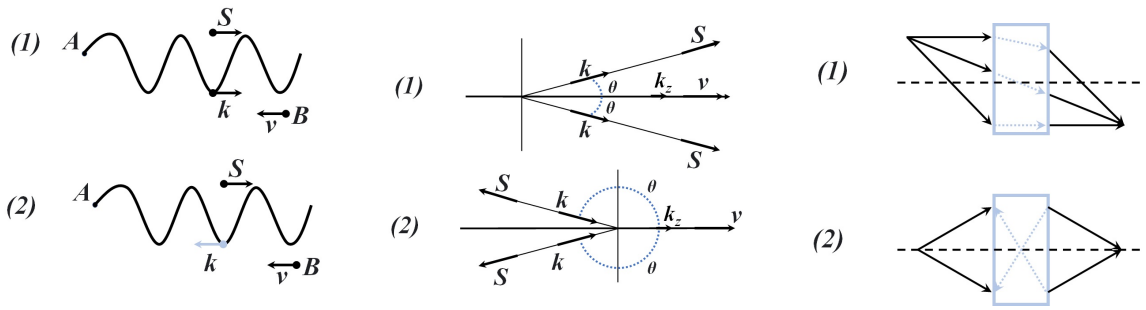

(a) Doppler effect (b) Cerenkov radiation (c) Negative refraction

Figure 1.2: Visualization of V.G. Veselago's phenomena of (a) a reverse doppler effect (b) an inverted Cerenkov radiation and (c) negative refraction. (1) represents the effects of a right-handed substance vs. (2) the effects of a left-handed substance on a scattered wave.

It wasn't until the early 2000s when physicist J.D. Pendry set out to create 'the perfect lens' based on theories and concepts from Veselago. The lens would have "the power to focus all Fourier components of a two-dimensional image, even those that do not propagate in a radiative manner" [7]. Pendry's biggest challenge dealt with focusing the amplitude of evanescent waves as they moved away from an object instead of correcting their phase due to their natural decay in amplitude without phase change. The premise of the lens would have a material with negative material constituents, ε = -1 and μ = -1, similar to the dielectric response of plasma and magnetic plasma, respectively. He proved this feat with a simulation of a thin slab of silver with thickness, d, that would provide the space for focusing the amplitude of the decaying evanescent waves. This lens shows in a similar sense to Veselago's diagram of negative refraction (Fig. 1.2c). Pendry concluded his paper by introducing a structure made up of a set of metallic rings that would provide negative permeability.

About a year later, D.R. Smith used Pendry's conclusion and assembled his 'split ring resonator (SRR).' Based on the findings and theoretical concepts of Veselago and Pendry, his group constructed a medium that operated in the microwave region with negative permeability and permittivity values, simultaneously. They achieved this by assembling periodic combinations of metallic rings with gaps with a continuous

line of wires. The nonmagnetic splint rings provided negative permeability, while the wires provided negative permittivity [1]. The SRR is composed of two split loops, one inside the other. The openings of the loop are located on opposite sides of each other to generate a large capacitance in the area between the rings. The resulting capacitance lowers the resonant frequency to focus the electric field. Using split rings allows the SRR unit to be resonant are wavelengths that are larger than the loop diameter. Smith fabricated the SRR using square arrays of the design with spacings in between each element. The split-ring resonators can bBased on his findings, e seen in Fig. 1.3b as well as the whole metamaterial in Fig. 1.3a.

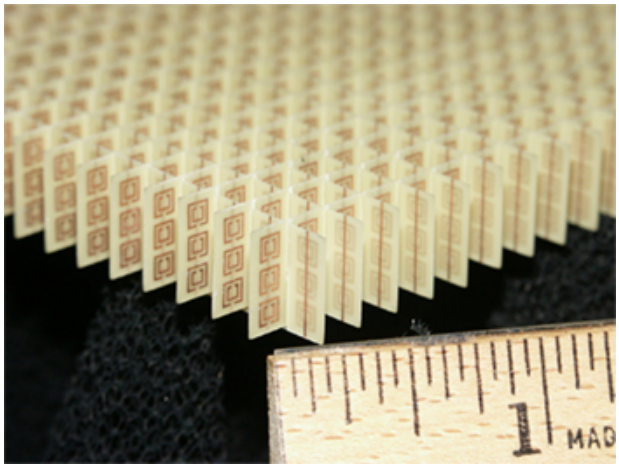

(a) Left-handed medium built by D.R. Smith.

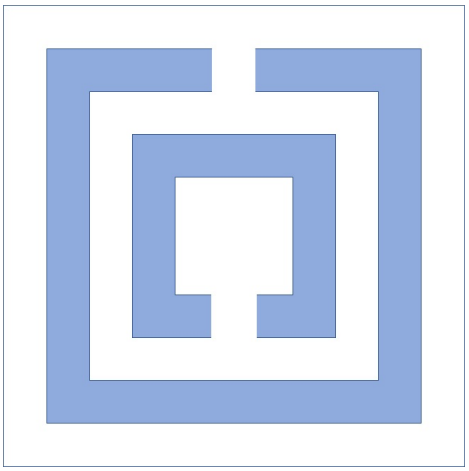

(b) Split-ring resonator used in the left-handed medium.

Figure 1.3: (a) Photo of the first 'Left-handed medium' constructed by D.R. Smith. The medium consists of a periodic combination of metallic rings with gaps, or split-ring resonators, which provides negative permeability and continuous wires, providing negative permittivity. (b) The split-ring resonator is comprised of two nonmagnetic loops with splits at opposite ends [1].

1.3 Metasurface Antenna Review

Being lightweight, low profile, and inexpensive, the application of antennas constructed with metasurfaces was inevitable. A metasurface antenna is a type of antenna that uses a metasurface to control the radiation pattern of the antenna. By carefully designing the metasurface, the antenna can be made to radiate waves in a specific

direction or to focus the waves into a beam. Metasurface antennas are already being used in a variety of applications and are being studied to determine specific outcomes, such as parameter control, allowing dual frequency, and having multiple beams.

1.3.1 Controlled Amplitude, Phase, and Polarization

Minatti et al. paved the way by developing a procedure for synthesizing modulated metasurface antennas with target amplitude, phase, and polarization. The synthesis process starts by setting the initial values of the wave number and size of the antenna based on the desired operating frequency, medium, and thickness. These parameters are then used in an iterative loop derived from analytical formulas derived by an adiabatic Floquet-wave expansion of currents and fields over the desired surface to determine the antenna characteristics [8]. They even included a troubleshooting section, if the process failed to converge. Using their method, they synthesized four examples of antennas with different desired outcomes, a circularly polarized (CP) elliptical beam, a CP sectorial bilateral isoflux beam, a CP sectorial monolateral isoflux beam, and a linearly polarized broadside beam and measured the resulting maximum gain, pattern, and cross-polar levels. The types of antennas were chosen based on their real-life application including space communications. Their results not only provided at least 85% efficiency, but they were able to conclude that polarization control is based on the local value of the anisotropy, the phase is controlled by both the shape and the periodicity of the modulation, and the amplitude control is obtained by designing the local leakage distribution of a leaky wave.

1.3.2 Dynamic Metasurfaces

Metasurfaces provide a huge platform in future technology due to their low-cost, lightweight, and low profile. Boyarsky et al. considered taking this a step further with the application of dynamic metasurface antennas (DMA) to synthetic aperture radar (SAR) systems. Traditional SAR technologies rely on phased arrays and me-

chanically steered systems to implement tailored electromagnetic waves. Boyarsky reveals that electronically tuned DMAs can provide the means for steerable, directive beams without the aid of mechanical components. The grounds of their design use consist of a metasurface comprised of individually addressable elements, with the overall radiation as a superposition of the fields generated by each element. The two implementation strategies to address the elements were binary and grayscale. Binary is based on either turning the element from a radiation (on) state to a non-radiating (off) state. Grayscale refers to applying a change in the resonance of the elements. Their goal was to demonstrate and provide the means for a DMA, rather than fabrication, presented a sample metasurface aperture comparable to traditional SAR systems. [9]

1.3.3 Implementation of Various Textures

Faenzi et al. provided various prototypes of MTS antennas that were constructed with different textures and geometry parameters. The texture designs included: (1) coffee bean, (2) grain of rice, (3) patch with slot, (4) patch with cross slot, (5) double π, and (6). (1), (2), and (6) can be referenced in Fig. 1.4a, Fig. 1.4b and Fig. 1.4c, respectively, along with a view of the input port. The remaining textures can be referenced in Fig. A.2, of the appendix. They go about in great detail about the electromagnetic models that were used during the analysis of their multiple antennas. These models include the continuous anisotropic reactance model, the Adiabatic Floquet modes model, a Gaussian-Ring basis function for Method of Moments analysis by continuous boundary conditions, the synthesis of the subwavelength printed elements, and the fast multipole method analysis. After the analysis of the antennas, certain realizations were considered based on their resulting EM performances. The results provided possible applications in which each design would be featured best, such as anisotropy control, the range of the reactance, the bandwidth, sensitivity to tolerances, and losses in the metal. They proved that by tailoring the shape of the

textures, the antennas can be easily reconfigured to provide desired outcomes. Their implementations showed experimentally to have an aperture efficiency of up to 70% [2].

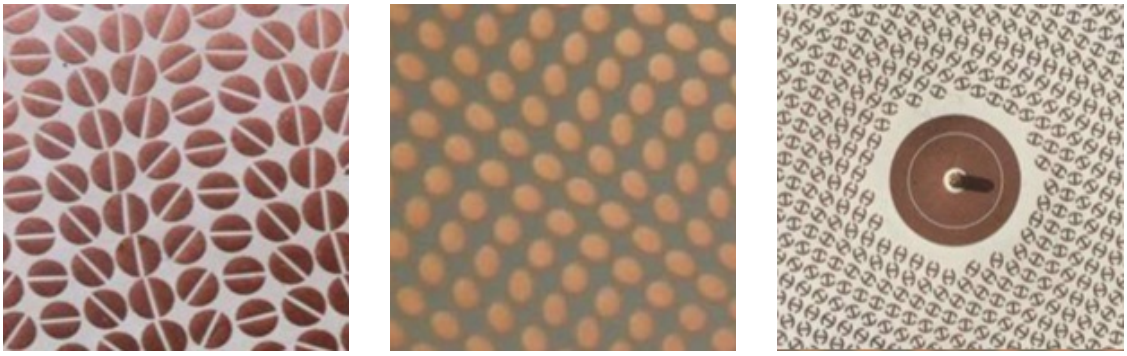

(a) (b) (c)

Figure 1.4: Examples of textured layout for implementing the MTS: (a) coffee bean (b) grain of rice and (c) double anchor and details of the feed [2].

1.3.4 Supporting Dual-Frequency

Using a similarly methodical approach, Li et al. proposed various configurations for compact metasurface antennas that support dual-band operations with Characteristic Mode Analysis (CMA). CMA is a method of analyzing the electromagnetic behavior of a system by breaking down a system into its constituent components and studying their individual electromagnetic characteristics under a wide range of conditions such as operating frequency, amplitude, and phase. Dual-band and multiband antennas have been the latest trend in the development of wireless communication technologies and the implementation of CMA to configure metasurfaces to support dual-band applications led Li et al. to their research. They defined the design of a patch-based metasurface, a modified metasurface, and a modified metasurface with malta cross-shaped edge patches and determined which modes could be used to achieve dual-band.The outcome resulted in a single-layered metasurface with an array of modified 3x3 square patches, fed with a single Y-junction feed that operated at 26.5 GHz and 38.9 GHz with 90 percent radiation efficiency while keeping a low profile ($1/5\lambda_{SW}$)

[3]. This metasurface as well as the researched design can be referenced in Fig. 1.5.

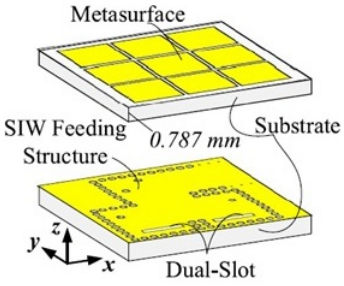

(a) Configuration of the patch-based metasurface antenna.

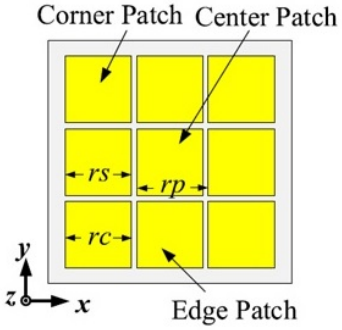

(b) Patch-based metasurface.

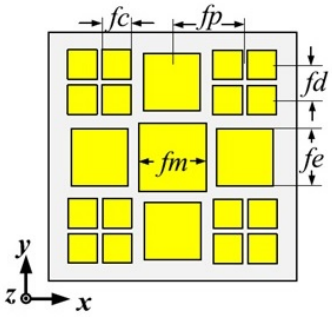

(c) Modified metasurface.

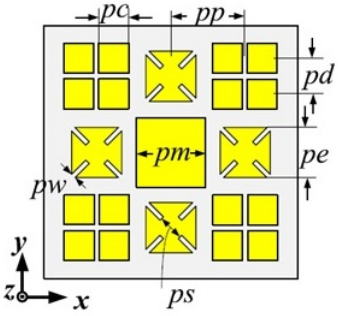

(d) Modified metasurface with Maltese cross-shaped edge patch.

Figure 1.5: Configuration of the proposed metasurface and antenna by Li et al. [3].

1.3.5 Multi-beam Antennas

Using Li et al.'s research with single metasurfaces, Wang et al. fabricated a single-fed four-beam reflector antenna by combining a phase gradient surface superimposed with a surface resembling a coding sequence. The phase gradient surface is implemented to provide a focused beam while the coding sequence supplied the means for multiple beams. Three different phase-coding sequences were used to develop the circular-polarized reflector antennas. They used the 0101.../0101...coding sequence for a double-beam antenna, the chessboard coding sequence for a four-beam antenna, and a 1-bit sector coding sequence for an eight-beam antenna. By using sequences

and patterns with binary digits, Wang et al. open the door for future configurations of multi-beam patterns through computer programs. A visual of the phase gradient surface and the chessboard coding sequence surface can be seen in Fig. 1.6. The figure shows their individual radiation patterns and the union of the two surfaces. This resulted in an antenna that produced four perfect pencil-shaped beams in a frequency range of 11 to 13 GHz [4]. The configuration of the 0101.../0101...coding sequence and 1-bit sector coding sequence can be seen in Fig. A.1 of the appendix.

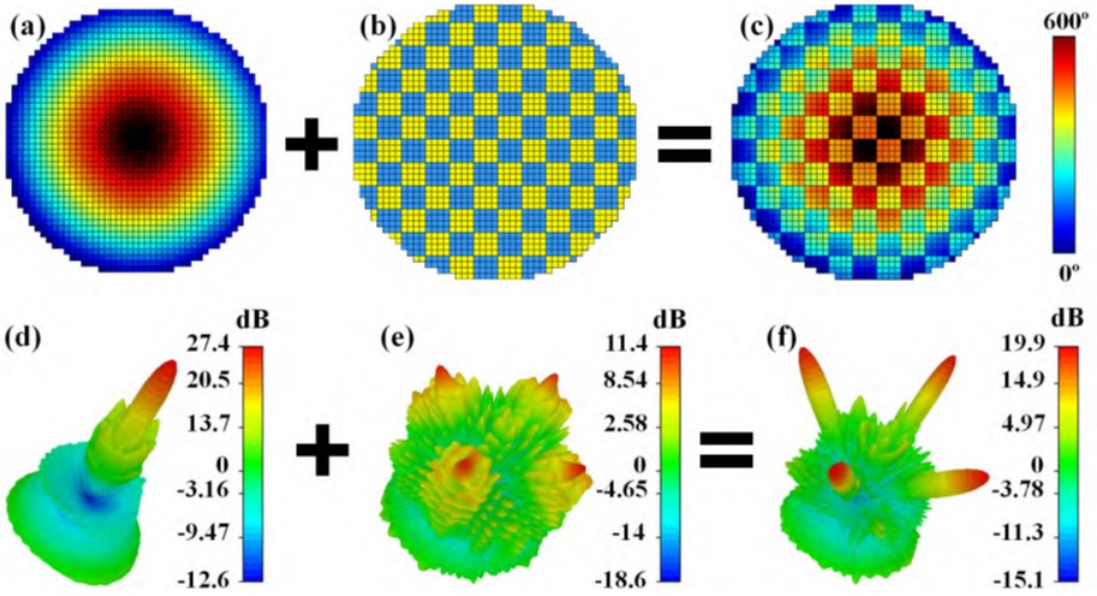

Figure 1.6: Phase distribution and simulated far-field radiation pattern of (a),(d) focusing metasurface; (b),(e) chessboard metasurface; (c),(f) superposition metasurface, respectively [4].

1.3.6 Wearable MTS Antennas

Antennas have evolved in the last decade and have seen rampant growth with the implementation of metasurfaces. Chaouche et al. presented the idea of an innovative wearable metasurface antenna operating in the wireless body area network. Currently, textiles, papers, polyester films, and ultra-thin polyimides are in use for their flexible characteristics but have seen significant drawbacks due to their low efficiency. The methodology of the wearable MTS by Chaouche et al. consists of a layer with a peri-

odic structure of electrically small resonators mounted to a layer of flexible RO5880 substrate, a layer of feeding networks connected by one feed port also mounted on a layer of RO5880 substrate, each connected to opposite sides of a ground plane. The prototype was fabricated and tested in free space, and on-body (chest, leg, and arm) operated at a range of 5.66 - 5.85 GHz. The measured gain reached a maximum of 12.82 dBi with a total efficiency of 79.93%. This type of MTS antenna is promising in many fields, such as health care, sports, and rescue operations. A wearable MTS antenna would be able to measure vital signs, pulse rates, glucose levels, and blood pressure instantaneously and simultaneously, eliminating the need for multiple specialized machines and providing ease for both the healthcare provider and the patient. [10]

1.4 Thesis Structure

The firTextilesthesis covers an introduction to metasurfaces, starting with an explanation of metamaterials, advantages, and possible applications. The history of metamaterials is discussed with the theories and research of Veselago, Pendry, and Smith. The following section revisits recent milestones and discoveries relating to metasurfaces, and the last section is the thesis structure.

Chapter 2 explains the theories and principles of surface waves, aperture antennas, metamaterials, modulated surface impedance, and leaky waves. Each section goes into detail, describing the behavior of electromagnetic waves with medium changes. These topics set the notion of which the reconfigurable metasurface antenna is designed.

Chapter 3 presents the design and analysis of the metasurface antenna, starting with a single unit cell. A database of the unit cell with different-sized apertures and the corresponding impedance is created and used to create a surface with a periodic arrangement of apertures with a specific average impedance. The surface is simulated under various changes, and the results are presented and discussed.

The last chapter presents the conclusion of the thesis and describes possible appli-

cations for the antenna.

CHAPTER 2: MODULATED METASURFACE ANTENNA

This chapter discusses all fundamental theories and concepts relating to a design of a modulated metasurface antenna. Section 2.1 will cover surface waves by defining electromagnetic waves and surface impedance through an explanation of the boundary conditions and the laws of reflection and refraction. Section 2.2 discusses aperture antennas through the field equivalence principle and gives an in-depth explanation of the radiation equations used with square/rectangular aperture antennas. Section 2.3 goes over the properties of metamaterials, including the idea of a negative refractive index and the configuration. Section 2.4 explores modulated surface impedance, through an explanation of tangential surface impedance and modulated metasurfaces. Lastly, section 2.5 of this chapter will introduce leaky waves and uncover the parameters for beam steering.

2.1 Surface Waves

This section explores the response of an electromagnetic wave at the boundary of two different composite mediums. The two mediums forge a surface at the interface and the behavior of the wave is described using theories, laws, and conditions.

2.1.1 Electromagnetic Waves

Electromagnetic (EM) waves are a type of energy wave that is emitted by electrically charged particles. These waves can travel through the vacuum of outer space, as well as through matter. They are made up of oscillating electric, **E**, and magnetic, **H**, fields and can travel at the speed of light. Two commonly used types of electromagnetic waves are transverse electric (TE) waves and transverse magnetic (TM) waves, which describe which field is perpendicular to the direction of propagation of

the wave. The study of electromagnetic waves uses these fields called 'plane waves' that describe the wave [5]. These fields can be described as

$$\mathbf{E} = \mathbf{E}_0 e^{j\mathbf{k}\cdot\mathbf{r}} \quad [\mathrm{V/m}] \tag{2.1}$$

$$\mathbf{H} = \mathbf{H}_0 e^{j\mathbf{k}\cdot\mathbf{r}} \quad [\mathrm{A/m}] \tag{2.2}$$

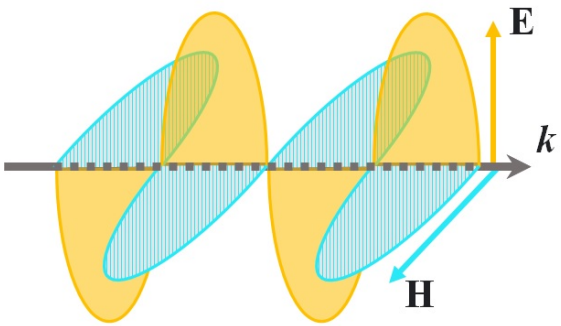

(a) Visualization of an electromagnetic wave represented by the wave vector **k**.

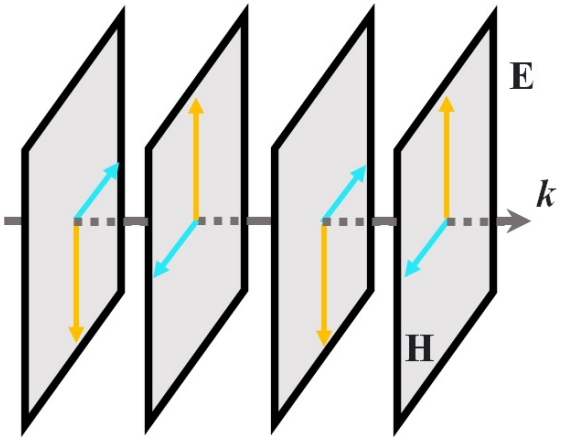

(b) Visualization of the plane waves that are used to study electromagnetic waves of wave vector **k**.

Figure 2.1: The electric, **E**, and magnetic, **H**, fields are represented in both figures with yellow and blue respectively. (a) The fields can be seen oscillating, tangential to each other, and normal to the wave vector. (b) Conversely, the fields are represented as vectors on a plane.

The fields are represented by a constant complex vector, $\mathbf{E}_0$ and $\mathbf{H}_0$, and wave vector, $\mathbf{k}\cdot\mathbf{r}$, with k representing the wave number and a point in space, r. The

electric field is measured in the SI unit, Volts per meter, (V/m) and similarly, the magnetic field is measured in Amperes per meter (A/m). For normal waves, the electric and magnetic fields follow the convention of the right-hand rule where they are perpendicular to each other and normal to the direction of the source propagation. The relationship can be described using the source-less Maxwell Equations and the absolute permittivity and permeability are ε and μ, respectively.

$$\nabla \times \mathbf{E} = -j\omega\mu\mathbf{H} \tag{2.3}$$

$$\nabla \times \mathbf{H} = j\omega\varepsilon\mathbf{E} \tag{2.4}$$

For explanation purposes of all instances, unless specifically defined, time-harmonic fields and waves will be assumed. The time variation is sinusoidal and using time-harmonic convention, $e^{-j\omega t}$, the angular frequency is represented as $\omega = 2\pi f$. The use of $\hat{\mathbf{n}}$ or $\mathbf{n}$ denotes a unit vector normal to the surface. Also, ε is the absolute permittivity of a material, which equals the relative permittivity of the material, ε_r, and free space permittivity, ε_0. Similarly, the absolute permeability of a material, μ, equals the relative permeability of the material, μ_r, and free space permeability, μ_0.

$$\varepsilon = \varepsilon_r\varepsilon_0 \tag{2.5}$$

$$\mu = \mu_r\mu_0 \tag{2.6}$$

The behavior of electric and magnetic fields can be described using their wave numbers in the generic form,

$$k = \beta - j\alpha \tag{2.7}$$

where k, is the wave number, β represents the phase constant [rad/m] and α is the attenuation constant [Np/m]. The phase constant represents the change in phase per unit length and the attenuation describes the change in the amplitude of the wave

[11].

2.1.2 Impedance Boundary Conditions

The composition of a material allows for the scattering of EM waves and the interaction between two different materials causes EM waves to behave differently. These waves can be studied and calculated using the impedance boundary conditions (IBC). These simplify and take into account the surface in which the electromagnetic field is incident to another medium. Without these simplifications, the field expansion in and outside of the material would need to be calculated [12]. IBC are based on concepts formulated from Maxwell's equations and take into account all of them in terms of the surface.

Exact boundary conditions occur at the interface of two homogeneous isotropic mediums that are not perfectly conducting. When IBCs examine the interface of a PEC or PMC and air (free space), the initial conditions reduce to

$$\hat{\mathbf{n}} \times \mathbf{E} = 0 \tag{2.8}$$

$$\hat{\mathbf{n}} \times \mathbf{H} = \mathbf{K} \tag{2.9}$$

$$\hat{\mathbf{n}} \cdot \mathbf{D} = \delta \tag{2.10}$$

$$\hat{\mathbf{n}} \cdot \mathbf{B} = 0 \tag{2.11}$$

where δ is the surface distribution, $\mathbf{K}$ is the current distribution, $\mathbf{B}$ is the magnetic flux density, and $\mathbf{D}$ is the electric flux density. Magnetic flux is related to the magnetic field by $\mathbf{B} = \mu\mathbf{H}$ and measured in Webers per square meter ($\mathrm{Wb/m^2}$) or Teslas (T). Similarly, electric flux density is related to the electric field by $\mathbf{D} = \varepsilon\mathbf{E}$ and is measured in Coulombs per meter squared ($\mathrm{C/m^2}$). The complex ε and μ is used in calculations [13]. These conditions allow us to conclude that the tangential electric field, $\mathbf{E}_t$, the normal magnetic flux density, $\mathbf{B}_n$, the normal electric flux density, $\mathbf{D}_n$

and the tangential magnetic field, $\mathbf{H}_t$ are all continuous.

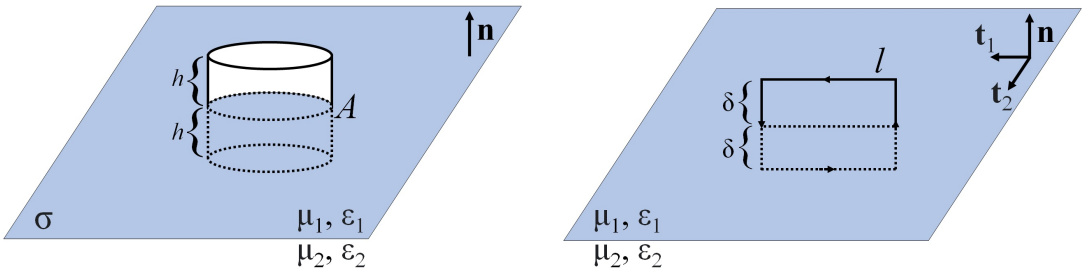

(a) Visualization of the IBC, relating to Gauss' law, referencing a 'tube' and enclosed surface A.

(b) Visualization of the IBC, relating to Faraday's law, using a closed loop of length l.

Figure 2.2: Illustration of the foundation of the impedance boundary conditions with two mediums of different permittivities and permeabilities, separated by a surface noted by the gray area. Both instances start out with concepts of Maxwell's equations to describe the interaction and the resulting EM waves between the two mediums.

2.1.3 Law of Reflection and Law of Refraction (Snell's Law)

The refractive index states a material's light-bending ability or how much energy or light is warped when entering a material [14]. The absolute refractive index of a material, n is the ratio of the materials phase velocity, v, and the speed of light, c ($n = c/v$). This property is the basis for both the law of reflection and the law of refraction.

The law of reflection and the law of refraction, which is also referenced as Snell's law, take into account the boundary conditions and describe wave behavior in relation to the surface of two mediums. To describe these two laws, a plane wave is assumed with wave vector, $\mathbf{k}_i$. This wave is incident from a material with refractive index n_1 (> 0) into another material with refractive index n_2 (> 0). At the boundary where both of the materials meet, part of the wave is reflected, $\mathbf{k}_r$, while another part is transmitted, $\mathbf{k}_t$, into the second material [14]. These wave vectors can be written with their corresponding components as

$$\mathbf{k}_i = k_i(\hat{\mathbf{x}} \sin\theta_i + \hat{\mathbf{y}} \cos\theta_i) \tag{2.12a}$$

$$\mathbf{k}_r = k_r(\hat{\mathbf{x}}\sin\theta_r - \hat{\mathbf{y}}\cos\theta_r) \tag{2.12b}$$

$$\mathbf{k}_t = k_t(\hat{\mathbf{x}}\sin\theta_t + \hat{\mathbf{y}}\cos\theta_t). \tag{2.12c}$$

The electric field will be occurring on the same plane of incidence. The polarization of these waves is referred to as 'p-polarization,' referring to the transverse magnetic state, and will be studied in examples. The electric field of these waves can then be expressed as correspondents of the wave vectors with equations 2.13.

$$\mathbf{E}_i(\mathbf{r}) = \mathbf{E}_{0i}e^{j\mathbf{k}_i\cdot\mathbf{r}} \tag{2.13a}$$

$$\mathbf{E}_r(\mathbf{r}) = \mathbf{E}_{0r}e^{j\mathbf{k}_r\cdot\mathbf{r}} \tag{2.13b}$$

$$\mathbf{E}_t(\mathbf{r}) = \mathbf{E}_{0t}e^{j\mathbf{k}_t\cdot\mathbf{r}} \tag{2.13c}$$

As stated in the previous section, the tangential components of $\mathbf{E}$ and $\mathbf{H}$ are continuous and the behavior of the electric fields at the interface of the two mediums is described with Eq. 2.14a.

$$E_{0i}\cdot\mathbf{t}e^{j\mathbf{k}_i\cdot\mathbf{r}}|_{y=0} + E_{0r}\cdot\mathbf{t}e^{j\mathbf{k}_r\cdot\mathbf{r}}|_{y=0} = E_{0t}\cdot\mathbf{t}e^{j\mathbf{k}_t\cdot\mathbf{t}}|_{y=0} \tag{2.14a}$$

For Eq. 2.14a to hold true for all values, the wave terms need to be equal, as stated in Eq. 2.14b. This simplifies and reveals that the transverse projections of all the wave vectors are equal to each other (eqn. 2.14c).

$$\mathbf{k}_i\cdot\mathbf{r}|_{y=0} = \mathbf{k}_r\cdot\mathbf{r}|_{y=0} = \mathbf{k}_t\cdot\mathbf{r}|_{y=0} \tag{2.14b}$$

$$k_i\sin\theta_i = k_r\sin\theta_r = k_t\sin\theta_t \tag{2.14c}$$

The law of reflection refers to the relationship between the incident wave and the reflected wave at the boundary between two mediums [14]. Since the wave terms are equal, it equates k_i to k_r, resulting in Eq. 2.15b. Both of the remaining angles have a range of 0 to $\pi/2$, which can be simplified one step further, revealing the law of reflection (Eq. 2.15c). This relationship is one of the key concepts in electromagnetics and physics due to its vast range of implementations.

$$k_i \sin\theta_i = k_r \sin\theta_r \tag{2.15a}$$

$$\sin\theta_i = \sin\theta_r \tag{2.15b}$$

$$\theta_i = \theta_r \tag{2.15c}$$

Equation 2.14c also sets up the relation and equation describing the behavior of the incident wave, $\mathbf{k}_i$, and the transmitted wave, $\mathbf{k}_t$.

$$k_i \sin\theta_i = k_t \sin\theta_t \tag{2.16a}$$

Since these two waves occur in two different mediums, the relation $k_i = n_1\omega/c$ and $k_t = n_2\omega/c$ relates the waves to their wave numbers to the refractive index of their respective mediums. This relation reveals the law of refraction, also known as Snell's law. These two laws can be referred to in Fig. 2.3.

$$n_1 \sin\theta_i = n_2 \sin\theta_t \tag{2.16b}$$

2.1.4 Surface Impedance

When a propagating EM wave is constrained to the boundary of two mediums, it is referred to as a surface wave. The wave is bound to the surface of the host medium

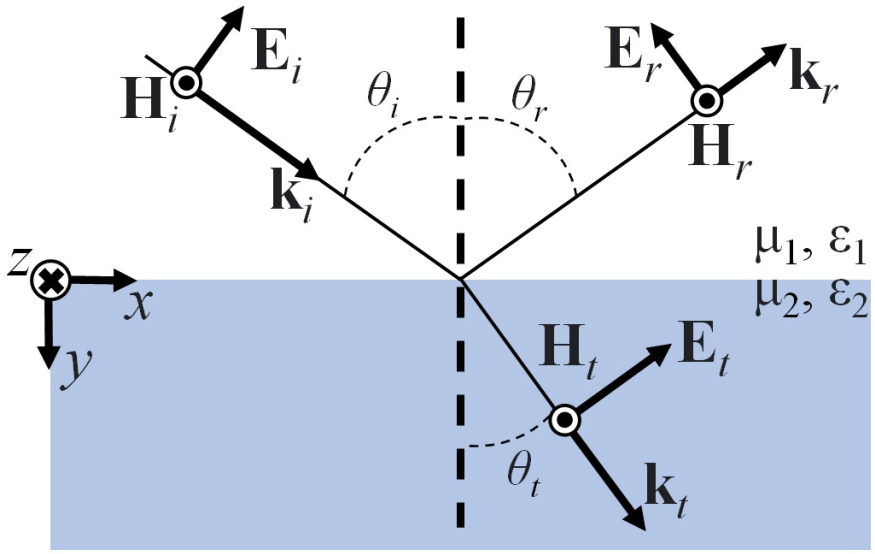

Figure 2.3: Diagram representing the law of reflection and the law of refraction, also known as Snell's law. Both laws use the concept of boundary conditions between two different mediums to describe the behavior of waves at the interface. The incident wave is represented by its wave vector, $\mathbf{k}_i$, and describes a p-polarization state for its fields. The resulting reflective and transmitted waves and their corresponding fields are represented as $\mathbf{k}_r$, and $\mathbf{k}_t$, respectively.

where it usually does not extend into the bulk of the material. The medium's surface composition provides an impedance (Ω) to the incident wave. If texture or alteration is added to the surface of the host medium, the surface impedance can be altered. This change to the impedance can be highly inductive or capacitive and on the magnitude of reactance, ultimately changing the properties of the surface wave.

Using the properties of the EM wave and the Maxwell equations, the surface impedance can be defined with a TM wave (Eq. 2.17) and a TE wave (Eq. 2.18) [15].

$$Z_{s,TM} = \frac{j\alpha}{\omega\varepsilon} \tag{2.17}$$

$$Z_{s,TE} = \frac{-j\omega\mu}{\alpha} \tag{2.18}$$

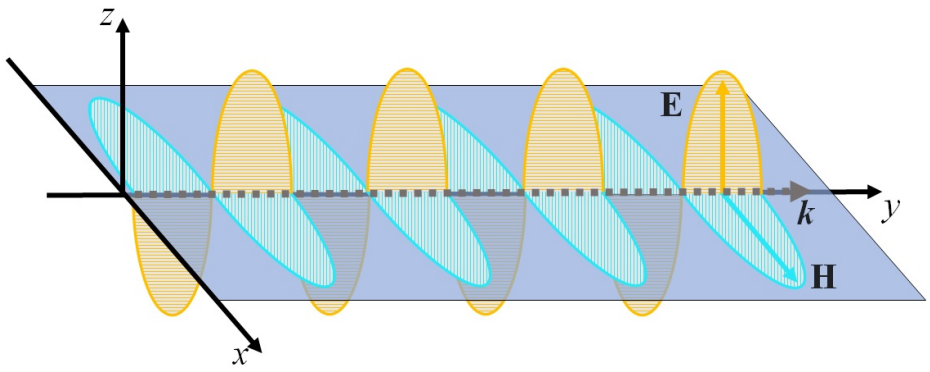

Figure 2.4: Visualization of an electromagnetic wave bound to a surface. The surface wave is represented by wave vector, $\boldsymbol{k}$, bounded to the surface in blue. Visualization is of a TM wave, where the magnetic field traverses across the surface.

2.2 Aperture Antennas

This section will discuss aperture antennas and their use of the Field Equivalence Principle to determine the radiation they will produce as well as how to describe the radiation [5].

2.2.1 Synopsis

At microwave frequencies, the use of aperture antennas is common and is the basis for this antenna design. It typically has a much higher gain and directivity than other types of antennas, making them ideal for applications such as wireless communication, radar, or satellite communications. The basic design of an aperture antenna consists of solid metal or dielectric material with an opening that emits electromagnetic waves. The aperture shape can be square, rectangular, circular, elliptical, or any other configuration that best fits the antenna's purpose. Examples of aperture shapes can be visualized in Fig. 2.5. Rectangular apertures are used for their commonality and practicality and will be used to illustrate behaviors and properties [16].

(a) Rectangular Aperture

(b) Circular Aperture

Figure 2.5: Examples of different shape aperture antennas. The physical antenna is represented in blue while the aperture is in the center of both examples.

2.2.2 Field Equivalence Principle: Huygen's Principle

The field equivalence principle is used to determine approximations of fields formulating around an antenna. It was introduced by S.A. Schelkuoff and is a derivative of Huygens' principle about spherical waves. This principle is based on the uniqueness theorem which correlates the unique properties of a field in a lossy determined by the sources within a region and its tangential components of the electric and magnetic field over a boundary [5].

Imagine a source, electrically represented by electric current density, $\mathbf{J}_1$ and magnetic current density, $\mathbf{M}_1$, encompassed by a defined surface, $\mathbf{S}$. The volume enclosed by $\mathbf{S}$ is defined as $\mathbf{V}_1$, and the surrounding volume, $\mathbf{V}_2$. The source radiates the electric, $\mathbf{E}_1$, and magnetic fields , $\mathbf{H}_1$, everywhere due to equal magnetic permeabilities, μ_1, and electric permittivities, ε_1. The premise of the equivalence principle is to replace the original source with a theoretical equivalent source that produces the same fields, $\mathbf{E}_1$ and $\mathbf{H}_1$, into $\mathbf{V}_2$.

In the equivalence problem, the fields $\mathbf{E}$ and $\mathbf{H}$ exist inside $\mathbf{S}$ while the fields $\mathbf{E}_1$ and $\mathbf{H}_1$ are outside of $\mathbf{S}$. If the tangential electric and magnetic field component boundary conditions are met, these fields exist and the equivalent sources, $\mathbf{J}_S$, and,

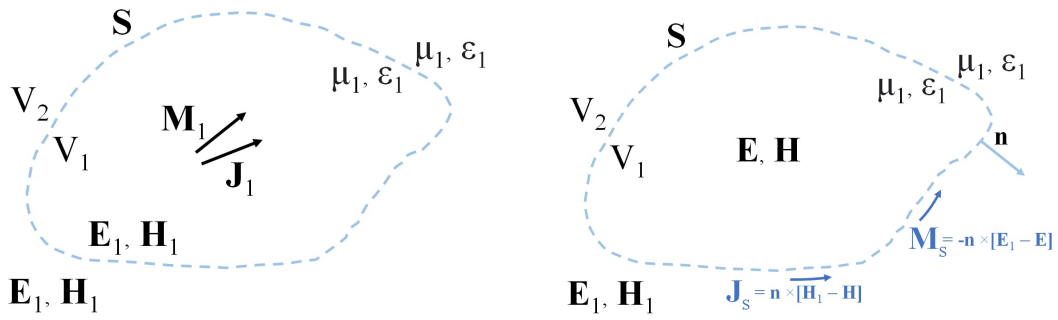

(a) Actual Problem

(b) Equivalent Problem

Figure 2.6: Models representing the Field Equivalence Principle. The actual problem (a) determines a surface, S, that has electric current density, $\mathbf{J}_1$, and magnetic current density $\mathbf{M}_1$. (b) shows the equivalent model of (a) that will produce the same fields outside of the surface as in the surface, so far field patterns can be studied.

$\mathbf{M}_S$, radiate into $\mathbf{V}_2$. Inside $\mathbf{S}$, $\mathbf{E}$ and $\mathbf{H}$ can be set to zero since it is not an area of interest, simplifying the equations into a form known as *Love's Equivalence Principle.* [5]

$$\mathbf{J_S} = \hat{\mathbf{n}} \times (\mathbf{E_1} - \mathbf{E})|_{\mathbf{H=0}} = \hat{\mathbf{n}} \times \mathbf{E_1} \tag{2.19}$$

$$\mathbf{M_S} = -\hat{\mathbf{n}} \times (\mathbf{H_1} - \mathbf{H})|_{\mathbf{E=0}} = -\hat{\mathbf{n}} \times \mathbf{H_1} \tag{2.20}$$

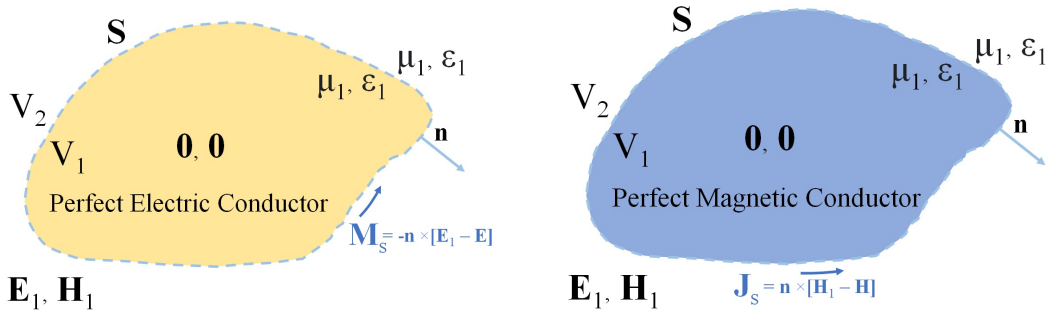

(a) Equivalence principle for a perfect electric conductor (PEC).

(b) Equivalence principle for a perfect magnetic conductor (PMC).

Figure 2.7: Equivalent principle models showing a (a) PEC and (b) PMC.

In the cases where $\mathbf{S}$ is a PEC ($\mathbf{J}_S = 0$) or PMC ($\mathbf{M}_S = 0$), Eq. 2.19 and Eq. 2.20 can be simplified using the image theory. This is based on the principle that

waves can be represented as a superposition of plane waves and is used based on the reflection and refraction of waves at interfaces [5].

$$\mathbf{M_S} = 2\mathbf{E_1} \times \hat{\mathbf{n}} \tag{2.21}$$

$$\mathbf{J_S} = 2\hat{\mathbf{n}} \times \mathbf{H_1} \tag{2.22}$$

2.2.3 Radiation Equations

In order to examine rectangular apertures, the electric field over the opening is assumed to be constant and can be quantified using the formula

$$\mathbf{E_a} = \hat{\mathbf{a}}_\mathbf{y} E_0 \quad -a/2 \leq x' \leq a/2, \quad -b/2 \leq y' \leq b/2 \tag{2.23}$$

where E_0 represents the magnitude of the electric field and a and b are the length and width of the aperture, respectively. For conventional use a $\geq$ b. Due to the radiation the antenna emits, the results are configured into spherical coordinates r, θ, and ϕ. The unit r represents the source point and is the distance from the origin, θ is the zenith angle, ranging from 0 to π, and ϕ is the azimuth angle, ranging from 0 to 2π. The primed coordinates (x', y', z' or r', θ', ϕ') indicate space occupied by the sources, as well as ψ being the angle between the source point, r, and the source's ϕ component on the surface, r'. A diagram of these parameters can be referenced in Fig. 2.8, with the metallic part of the antenna in blue and the aperture parameters identified with a gray border.

The main interest will be based on results in the far field, where the observation point, R, is far, far away, and the source point is assumed to be parallel with each other [5]. With this assumption, the far field can be approximated and simplified by stating $R \approx r - r' \cos\psi$, for phase variations and $R \approx r$, for amplitude variations.

On a Cartesian plane, if the electric field is propagating along $\hat{\mathbf{a}}_\mathbf{y}$ then the magnetic

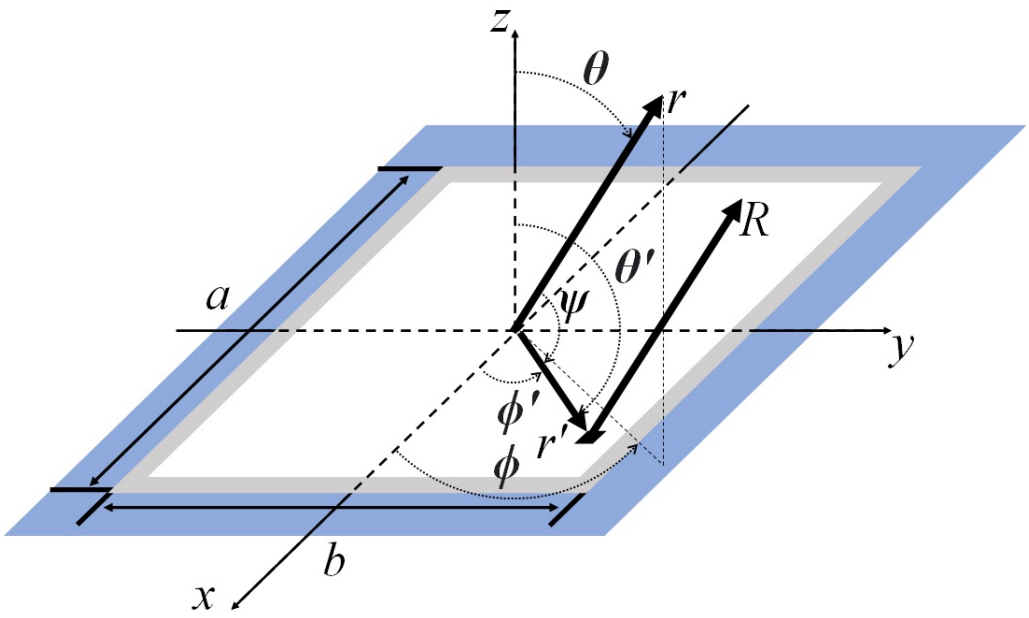

Figure 2.8: Diagram of a rectangular aperture antenna with aperture dimensions a and b. For far-field examinations the point source, r is far, far away from the observation point R. Primed coordinates indicate space occupied by the source as well as ψ being the angle between r and r'.

field will radiate along -$\hat{\mathbf{a}}_\mathbf{x}$, a concept defined by the RHR. Because of this relationship between the electric and magnetic field, the magnetic field over the aperture can be found using the formula

$$\mathbf{H_a} = -\hat{\mathbf{a}}_\mathbf{x}\frac{E_0}{\eta} \quad -a/2 \leq x' \leq a/2, \quad -b/2 \leq y' \leq b/2 \tag{2.24}$$

where $\eta = \sqrt{\mu/\varepsilon}$ is the characteristic impedance of the wave.

The radiation of the aperture in the far field can be described in terms of its spherical components. The electric field is defined by E_r, E_ϕ and E_θ and conversely, the magnetic field is described by H_r, H_ϕ, and H_θ. These components can be referenced in Fig. 2.8 and defined in Eq. 2.25 [5].

$$E_r = 0 \tag{2.25a}$$

$$E_\theta = j\frac{abkE_0e^{-jkr}}{2\pi r}\left[\sin\phi\left(\frac{\sin X}{X}\right)\left(\frac{\sin Y}{Y}\right)\right] \tag{2.25b}$$

$$E_\phi = j\frac{abkE_0e^{-jkr}}{2\pi r}\left[\cos\theta\cos\phi\left(\frac{\sin X}{X}\right)\left(\frac{\sin Y}{Y}\right)\right] \tag{2.25c}$$

$$H_r = 0 \tag{2.25d}$$

$$H_\theta = -\frac{E_\phi}{\eta} \tag{2.25e}$$

$$H_\phi = +\frac{E_\theta}{\eta} \tag{2.25f}$$

where,

$$X = \frac{ka}{2}\sin\theta\cos\phi \tag{2.25g}$$

$$Y = \frac{kb}{2}\sin\theta\sin\phi \tag{2.25h}$$

The electric field plane or 'E-plane,' contains the electric field vector and the direction of its maximum radiation. The E-plane is defined on the y-z plane, or $\phi = \pi/2$ rad, resulting in E_r and E_ϕ to equal zero. The E-plane is defined as,

$$E_r = E_\phi = 0 \tag{2.26a}$$

$$E_\theta = j\frac{abkE_0e^{-jkr}}{2\pi r}\left[\frac{\sin\left(\frac{kb}{2}\sin\theta\right)}{\frac{kb}{2}\sin\theta}\right] \tag{2.26b}$$

This equation was derived using an equivalent closed surface defined from -∞ to +∞ on the x-y plane and the integration of the space and element factors. The space and element factors describe a two-dimensional source distribution and the vector potential respectively.

The tangential relation between the electric and magnetic field allows the magnetic field plane or 'H-plane' to be derived from **E**. The H-plane is seen on the x-z plane

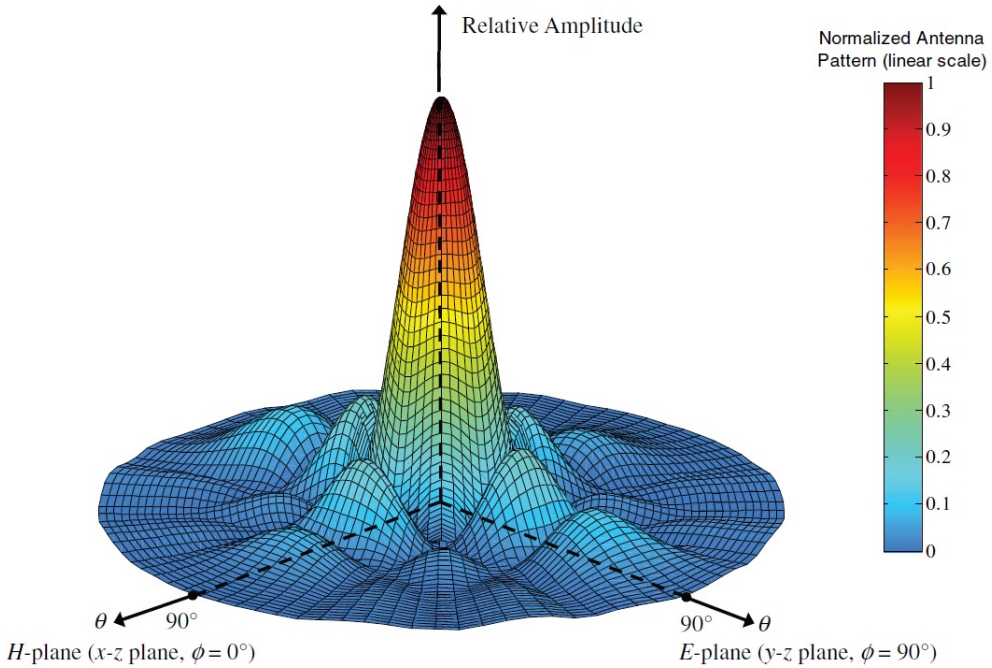

Figure 2.9: An example of a three-dimensional field pattern of a constant field square aperture mounted on an infinite plane [5].

or $\phi = 0$. Similarly, on this plane, H_r and H_ϕ equal zero, due to $H_r \sim E_r$ and $H_\phi \sim E_\theta$. The H-plane is defined as,

$$H_r = H_\phi = 0 \tag{2.27a}$$

$$H_\theta = -j\frac{abkE_0e^{-jkr}}{2\pi r\eta}\left[\cos\theta\frac{\sin\left(\frac{ka}{2}\sin\theta\right)}{\frac{ka}{2}\sin\theta}\right] \tag{2.27b}$$

The radiated fields of the aperture can be visualized in Fig. 2.9, showing both the E and H field.

The time average Poynting vector, $\mathbf{W}_{av}$, which is referred to more commonly, describes the average power density of an EM wave. It is derived from its instantaneous counterpart which describes the power and energy associated with an EM wave, in the general form $\mathscr{W} = \mathscr{E} \times \mathscr{H}$. $\mathscr{W}$ is the Poynting vector (W/m^2), $\mathscr{E}$ is the electric-field intensity, $\mathscr{E}$ is the magnetic field intensity, all at instantaneous times. The time

average Poynting vector is written as

$$\mathbf{W}_{av}(x,y,z) = [\mathscr{W}(x,y,z;t)]_{av} = \frac{1}{2}\mathrm{Re}(\mathbf{E}\times\mathbf{H}^{*}) \tag{2.28}$$

Radiated power, P_{rad}, uses the Poynting vector to measure the energy transmitted by an EM wave through a surface (Eq. 2.29a) [17]. It is measured in the SI unit, watts (W) which is a derivation of joules per second (J/s). This quantity uses the time average Poynting vector, resulting in P_{rad} to equal P_{av}, the average radiated power.

$$P_{rad} = P_{av} \tag{2.29a}$$

$$P_{rad} = \oiint_{S} \mathbf{W}_{av}\cdot ds = \oiint_{S} \mathbf{W}_{av}\cdot\hat{\mathbf{n}}da \tag{2.29b}$$

$$P_{rad} = \oiint_{S} \frac{1}{2}\mathrm{Re}(\mathbf{E}\times\mathbf{H}^{*})\cdot ds \tag{2.29c}$$

This equation can be simplified for rectangular apertures using the average power density of the wave, $|E_0|^2/2\eta$ through the surface and simplified further using the rectangular aperture dimensions seen in Eq. 2.29d.

$$P_{rad} = \frac{\left|E_0\right|^2}{2\eta}\iint_{S_a} ds = ab\frac{\left|E_0\right|^2}{2\eta} \tag{2.29d}$$

For rectangular apertures, the maximum radiation intensity, U_{max}, emitted usually occurs towards $\theta = 0$. It can be found relating the aperture dimensions, the wavelength, and the average power density.

$$U_{max} = \left(\frac{ab}{\lambda}\right)^2 \frac{\left|E_0\right|^2}{2\eta} \tag{2.30}$$

Directivity, D_0, is a measure of how well an antenna radiates in a particular direction in relation to the average radiated power it is emitting. The higher the directivity, the more focused the radiation is in that direction. For rectangular apertures, the directivity can be found in different ways based on the design parameters. A_p refers to the physical area of the aperture and A_{em} is the maximum effective area of the aperture. Since A_{em} is directly related to its maximum directivity, A_{em} and A_p are equal [17]. Directivity uses the decibel or dB and in certain instances, dBi is used, which is a decibel comparison to a theoretical isotropic antenna.

$$D_0 = \frac{4\pi}{\lambda^2}ab = \frac{4\pi}{\lambda^2}A_p = \frac{4\pi}{\lambda^2}A_{em} \tag{2.31}$$

Antenna efficiency, e_0 takes into account the losses within the antenna structure due to possible issues with impedance matching, e_r, conduction losses, e_c or dielectric losses, e_d. e_r refers to how well power is transferred from the feed network to the antenna or if there are any reflections due to a mismatch between the transmission line and the antenna. Conduction losses are ohmic losses that occur in the material that makes up the antenna while dielectric losses is related to the energy lost in the dielectric materials when waves travel through them. Usually, e_c and e_d are difficult to compute, so they are combined and referred to as e_{cd} but they can be determined experimentally [17]. The antenna efficiency is usually referred to as a percentage.

$$e_0 = e_r e_c e_d = e_r e_{cd} \tag{2.32}$$

The gain of an antenna, G_0, is the ratio of the power radiated in a given direction to the average power delivered to the antenna. When the direction is not stated the gain is usually taken in the direction of maximum radiation. It is closely related to directivity but takes into account the antenna efficiency as well [17]. Gain is measured

as a percentage dB, comparing the antenna to its efficiency.

$$G_0 = e_{cd} D_0 \tag{2.33}$$

2.3 Metamaterials

This section will cover the properties of metamaterials and why they are desirable for this application. The main focus will be on negative refractive index and an exploration of the configuration.

2.3.1 Negative Refractive Index

Negative index metamaterials have properties that reverse the propagation of EM waves and have a negative refractive index, n = -1. To explore this material, a plane wave is assumed with wave vector, $\mathbf{k}_i$. This wave is incident to a medium with $n_1 > 0$ into a second medium n_2 with constituent parameters, $\mu = \varepsilon = -1$. The behavior of the resulting wave, $\mathbf{k}_2$, is studied using the Maxwell equations and Snell's law.

$$\nabla \times \mathbf{E} = j\omega\mu\mathbf{H} \tag{2.34a}$$

$$\nabla \times \mathbf{E}_2 e^{j\mathbf{k_2}\cdot\mathbf{r}} = -j\omega\mu\mathbf{H}_2 \tag{2.34b}$$

$$\mathbf{k_2} \times \mathbf{E}_2 = -\omega\mu\mathbf{H}_2 \tag{2.34c}$$

$$\mathbf{H}_2 = -\frac{1}{\omega\mu}\mathbf{k_2} \times \mathbf{E}_2 \tag{2.34d}$$

The resulting magnetic field gives us insight into the relationship with the wave vector. Similarly, the electric field can be derived in the same way.

$$\mathbf{E}_2 = -\frac{1}{\omega\varepsilon}\mathbf{k_2} \times \mathbf{H}_2 \tag{2.35}$$

Both equations describe the relationship between the cross-product of the electric

and magnetic fields. Due to the material composition, the vectors form a left-handed tripod in contrast to a normal right-handed one [18], resulting in the phase 'left-handed media' or LHM.

$$\mathbf{k_2} \propto -\mathbf{E}_2 \times \mathbf{H}_2 \propto \mathbf{H}_2 \times \mathbf{E}_2 \tag{2.36}$$

This interaction can be described more in-depth with a new wave and Snell's law, Eq. 2.16b. For simplification purposes, $n_1 = 1$, which sets up the relation $n_1 = -n_2$.

$$n_1 \sin\theta_i = -n_1 \sin\theta_2 \tag{2.37a}$$

$$\sin\theta_i = -\sin\theta_2 \tag{2.37b}$$

$$\theta_i = -\theta_2 \tag{2.37c}$$

This equation simplifies in a similar fashion, leaving the angles of the resulting waves in relation to the boundary. It can be noted that the result of this interaction shows the sign of θ_2 reversed, resulting in negative refraction. Due to the boundary conditions, it can be noted that the Poynting vector, $\mathbf{W}_{av}$, is unchanged and can be seen going in the opposite direction as the refractive wave. These concepts can be visualized in Fig. 2.10, where k_2 and its constituents are replaced with a new delineation k_r, representing the refractive behavior of the wave.

The behavior of the waves coincides with all the related laws and conditions but the idea and math behind a negative index did not add up. Using the formal definition of the index of refraction, $n^2(\mathbf{r},\omega) = \varepsilon(\mathbf{r},\omega) \cdot \mu(\mathbf{r},\omega)$, it can conclude,

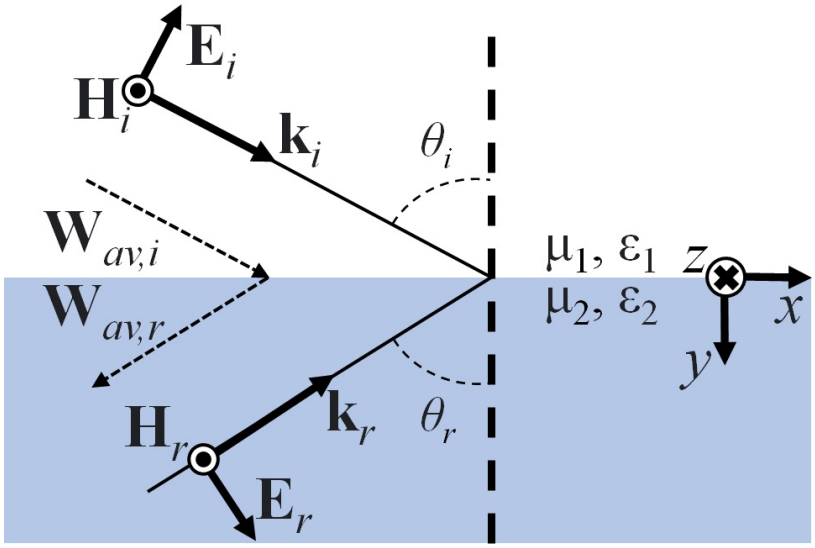

Figure 2.10: Diagram representing the law of refraction at the interface of two mediums, one of which index n_2 = -1. The incident wave is represented by its wave vector, $\mathbf{k}_i$, and describes a p-polarization state for its fields. The resulting refractive wave and corresponding fields are represented with $\mathbf{k}_r$ and designator, r.

$$\begin{aligned} n &= \pm\sqrt{\varepsilon\mu} \\ &= \pm\sqrt{(-1)(-1)} \\ &= \pm\sqrt{1} \\ &= \pm 1 \end{aligned} \tag{2.38}$$

In order for the index to be negative, the negative square root needed to be chosen. Pendry distinguished in his findings that both the ε and μ did not have to be negative in material to achieve a negative refractive index [7]. D.R. Smith's experiment revealed that the metallic rings were excited by an external alternating magnetic field resulting in a resonant magnetic dipole moment. The collection of magnetic dipoles led to resonant permeability,

$$\mu = \mu_0 \left(1 - \frac{F\omega}{\omega^2 - \omega_m^2 + i\omega\gamma_m}\right) \tag{2.39}$$

where ω_m is the radial frequency of the magnetic resonance, γ_m represents the losses and F, a geometrical factor. The negative permittivity was generated through a periodic system of thin metallic wires that when excited, behaved like a free electron plasma. The plasmon has a cut-off frequency of ω_p, which defines the cross-section of the wires and the periodicity of the medium [1]. This can be described as

$$\varepsilon = \varepsilon_0 \left(1 - \frac{\omega_p^2}{\omega^2}\right) \tag{2.40}$$

2.3.2 Metasurface Configuration

Periodic metamaterials are designed as three-dimensional volumetric structures or two-dimensional surface designs, metasurfaces. While there are many advantages and disadvantages to both, MTSs occupy less space and weigh less due to their low profile and lightweight design.

MTSs are described as high-impedance surfaces constructed on a solid metal ground plane. These high-impedance surfaces consist of small metallic patches or textures arranged periodically. The patches represent the original geometry on which the periodic structure is based upon. They are studied and configured using local periodicity assumptions, where the patches are infinitely repeating along a plane and have such a small gradual change among them that adjacent cells appear similar enough that there is no variation [2]. They then are then arranged in a periodic manner, resulting in the desired EM parameters.

To analyze and configure the effects of the patches and periodic arrangement on metasurfaces, surface impedance will be explored more in-depth. When the period is small compared to the target wavelength, the material can be analyzed as an effective medium. The surface impedance is equivalent to that of a parallel resonant LC circuit, with conductive (L) and capacitive (C) properties at its natural frequency, $\omega_0 = 1/\sqrt{LC}$. This analogy can be visualized in Fig. 2.11 [19]. The surface impedance

being described can be expressed as:

$$Z_s = \frac{j\omega L}{1 - \omega^2 LC} \tag{2.41}$$

To predict the reflective properties of a surface, a model of the LC circuit is used. The perspective parameters of the model need to be much much smaller than the wavelength being analyzed.

$$k^2 = \mu_0 \varepsilon_0 \omega^2 + \alpha^2 \tag{2.42}$$

The model and the surface impedance equations from earlier can be used to formulate

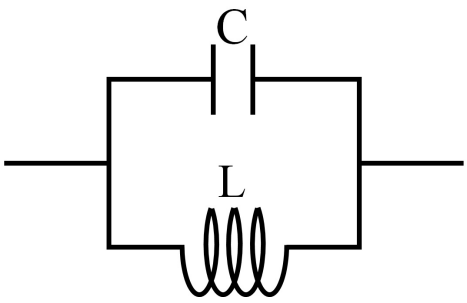

(a) LC circuit in parallel.

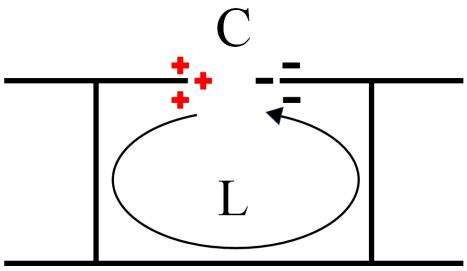

(b) Surface impedance represented as an LC circuit.

Figure 2.11: Materials can be analyzed as an effective medium when the period is smaller than the target wavelength. The surface impedance is equivalent to that of a parallel resonant LC circuit, with conductive (L) and capacitive (C) properties at its natural frequency.

the respective wave numbers for TM (Eq. 2.43) and TE (Eq. 2.44) waves.

$$k = \frac{\omega}{c}\sqrt{1 - \frac{Z_{s,TM}^2}{\eta^2}} \tag{2.43}$$

$$k = \frac{\omega}{c}\sqrt{1 - \frac{\eta^2}{Z_{s,TE}^2}} \tag{2.44}$$

Using the original wave number Eq. 2.7, the wave number and the relation $\beta = \omega\sqrt{LC}$, the phase constant of the wave on the metasurface can be described using, β_{SW}. This relation can be derived using Eq.2.45, where k_0 is the free space wave number, $\overline{X_s}$ is the average impedance of the surface and ζ is the free space impedance.

$$\beta_{SW} = k_0\sqrt{1 + \left(\frac{\overline{X_s}}{\zeta}\right)^2} \tag{2.45}$$

2.4 Modulated Surface Impedance

Modulated surface impedance describes a sinusoidal change in the impedance of a surface based on its location. This section covers the theories and concepts that encompass modulated surface impedance such as the impedance boundary conditions, surface waves, and surface impedance.

2.4.1 Tangential Surface Impedance

The tangential surface impedance can be related using the IBCs and information related to surface waves and surface impedance. This relates the average surface impedance, X_s, and both the electric and magnetic fields to their tangential components as seen in Eq. 2.46 [20].

$$\mathbf{E_t} = jX_s\hat{\mathbf{z}} \times \mathbf{H_t} \tag{2.46}$$

2.4.2 Modulated Metasurface

A smooth metasurface is assumed to have uniform impedance. This can be altered by adding texture or a periodic design, to fit the needs of the overall purpose of the surface. An example of a modulated metasurface by Dr. Mencagli's group can be seen in Fig. 2.12. The metasurface includes a circular, two-dimensional antenna with pins of varying heights to produce modular surface impedance. The impedance of a

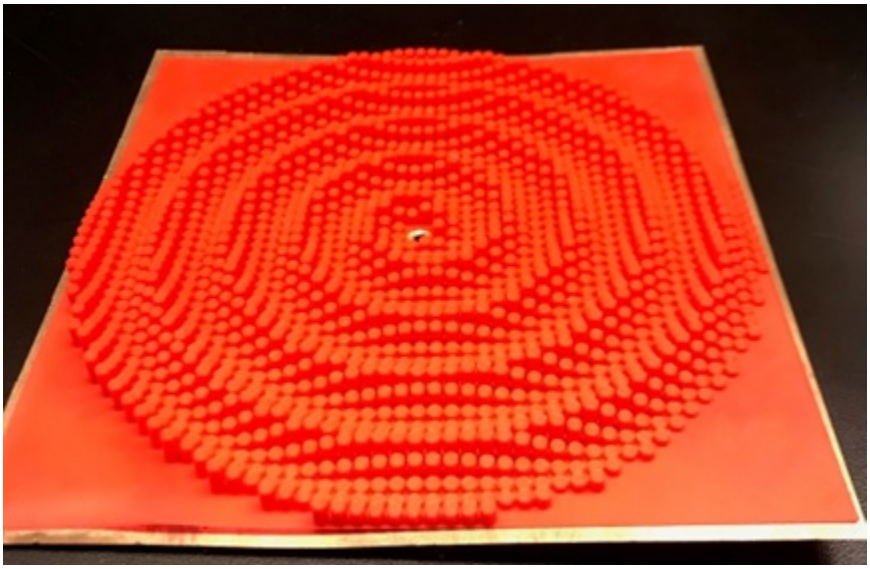

Figure 2.12: Example of modulated metasurface from Dr. Mencagli's group. This example shows a 3-D printed metasurface with the modulation occurring from different heights of the printed material.

one-dimensional modulated surface can be expressed as

$$X_s = \overline{X_s}\left[1 + M\cos\left(\frac{2\pi y}{d}\right)\right] \tag{2.47}$$

where M (> 0) is the modulation amplitude, and d is the period of modulation [21]. A uniform surface impedance has a modulation amplitude of 0 and is equal to the average surface impedance. The antenna design and simulation were created on the x-y plane. On this plane, the surface impedance modulation is one-dimensional along the y-axis, meaning the impedance of the surface will change with different y values

and will have this direct impedance value in the x direction.

2.5 Leaky Waves

This section will examine leaky waves through their improbable history due to being improper mathematically and lack of research. This section will also explain the physics behind leaky waves and the ability to beam steer.

2.5.1 Background

Leaky waves are electromagnetic waves that travel along a medium, such as a dielectric or a conductive surface. They are called 'leaky' because they leak power into the surrounding space as they travel. The amount of power that leaks out decreases with distance from the source, so leaky waves typically have a specified design to optimize the radiated power. Since these waves can be used for radiating or receiving purposes, they can be useful for directive antennas, where a strong beam of radiation is desired in a particular direction making them useful for communications.

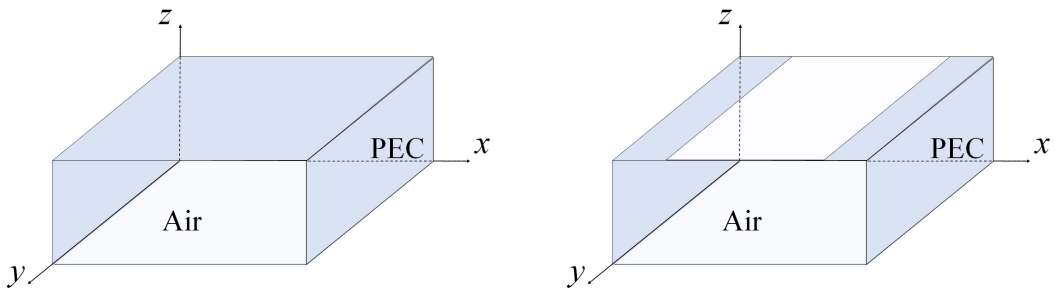

(a) Rectangular Waveguide

(b) Recreation of W.W. Hansen's Rectangular shut waveguide with a long uniform opening

Figure 2.13: Early research focused mainly on closed waveguides such as the rectangular one seen in (a) because they produced proper mathematically bounded waves. Hansen's rectangular waveguide (b) with a long uniform opening developed the environment for leaky waves.

These waves were deemed improper mathematically due to an increase in the transverse direction in comparison to bound waves, which decrease transversely. This idea was deterred from research due to the main and vast focus on closed waveguides and

the limited knowledge of leaky waves. In a closed lossless system, the eigenmodes have purely real or purely imaginary transverse wave numbers which represent propagating waves with constant amplitudes. It wasn't until the late 1930s when physicist W.W. Hansen proposed a rectangular shut waveguide with a long uniform opening and changed everything. This aperture provided the necessary means for the wave to escape and led to the creation of the first main leaky wave antenna.

2.5.2 Properties of Leaky Waves

An open waveguide will produce an effective antenna aperture for a traveling leaky wave. The far-field radiation pattern can be found by taking the Fourier transform of the aperture field. The leaking field on the aperture will have the complex longitude wave number $k_y = \beta$ - $j\alpha$, where β is the phase constant and α is the attenuation constant. This wave number will characterize the main features of its radiation pattern: direction of the main beam, beam width, and side lobe level.

When power is flowing in the positive longitudinal direction, a leaky wave with $\beta > 0$ will flow in that same direction, producing a forward leaky wave. Contrarily, a 'backward' leaky wave, moving in the opposite direction of the power flow, can be produced if $\beta < 0$. The attenuation constant or 'leakage constant,' α determines the angular width of the main beam and directly determines the effective antenna aperture, a large α will result in a short aperture and a wide beam while a small α will lead to a longer aperture and a narrow beam. Using this, the field above the aperture can be defined using the Helmholtz equation, by the transverse wave number [22].

$$k_z = \pm\sqrt{k_0^2 - k_y^2} = \beta_z - j\alpha_z \tag{2.48}$$

Physical sciences and electrical engineering use dispersion relations, which describe the effect of dispersion on the properties of waves in a medium, to relate the wave number of the surface to its frequency. Dispersion occurs when a wave travels through

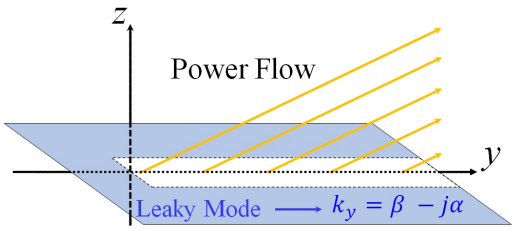

(a) Visualization of a forward leaky wave.

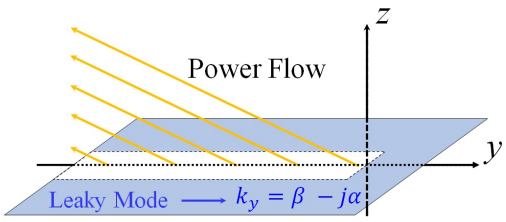

(b) Visualization of a forward leaky wave.

Figure 2.14: Both visualizations represent the effect the propagation constant, β, will have on leaky waves. If $\beta > 0$, the leaky wave will flow in the same direction of propagation, as seen in (a). Oppositely, if $\beta < 0$, the leaky wave will flow backwards to the direction of propagation.

a medium and the surface impedance causes a distortion among the harmonic waves, This may cause a breakdown and the waves may travel at different and various velocities. Using this relation, a dispersion curve can be used as a tool for propagating waves on a surface. An example dispersion curve can be seen in Fig. 2.15.

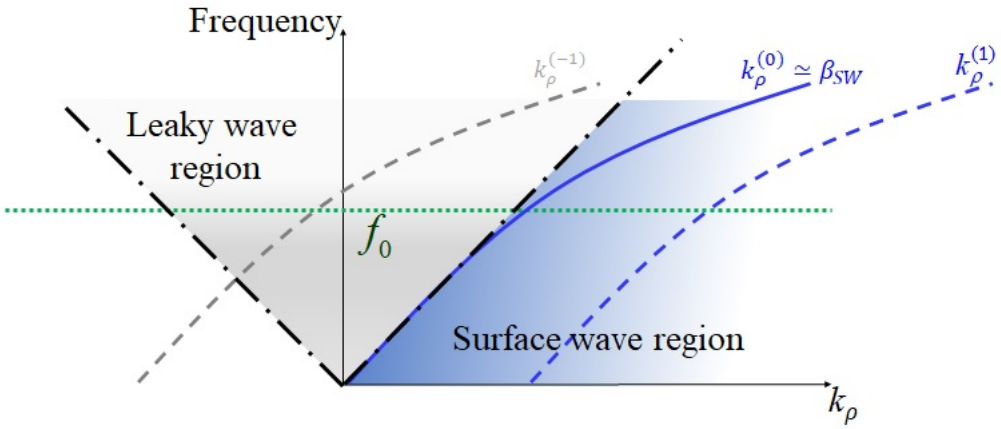

Figure 2.15: An example of a dispersion curve relating the wave number to its corresponding frequency. An arbitrary frequency f_0 is represented with the green dotted line. This specific curve compares the dispersion of waves with a negative refractive index, a positive refractive index, and a zero refractive index and the resulting regions of the waves.

Since a change in any of the surface parameters can cause a change in the average surface impedance and the corresponding wave number can be changed. A common

reference on dispersion curves is the 'light line.' The line represents an imaginary line based on the free space wave number, k_0, and splits the entire curve into two regions. If the real part of the resulting wave number is greater than k_0, the wave will be to the right of the light line in the surface wave region and will remain bounded. If it is less than the free space wave number, it will appear to the left of the light line and will appear in the leaky wave region, providing the space for a leaky wave. An arbitrary frequency f_0 can be seen as a green dotted line and used to follow if the following wave number will result in a leaky or surface wave at that frequency.

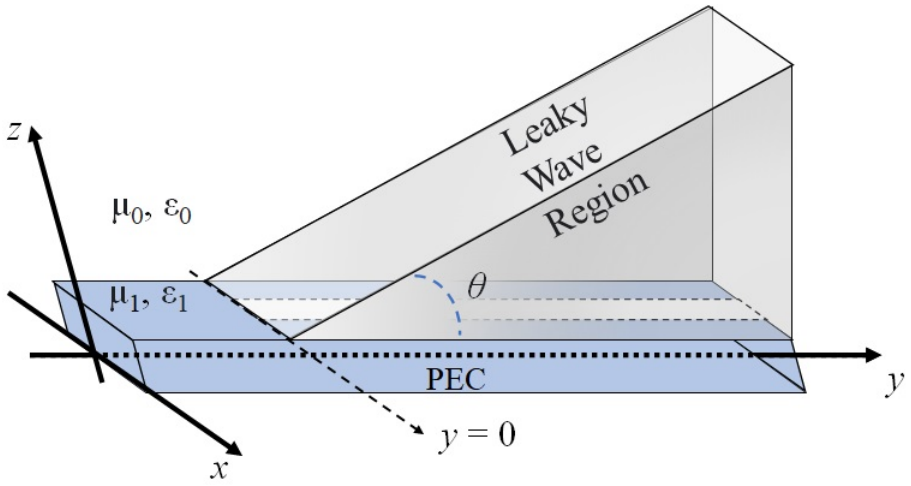

Figure 2.16: The leaky wave region describes a wedge-shaped area located over an aperture where leaky waves can occur. For a forward wave, the region is defined with $z < y \tan\theta$, where $y = 0$ determines the source location.

Leaky waves are defined only within a wedge-shaped region over the aperture emitting the wave based on the location of its source. For a forward wave, the leaky wave region can be defined using the inequality $z < y \tan\theta$, with the source placed at $y = 0$. The radiation angle of the leaky region can be found using

$$\theta = \tan^{-1}\left(\frac{Re[k_z]}{Re[k_y]}\right)\cos^{-1}\left(\frac{\beta}{k_0}\right) \tag{2.49}$$

where θ with respect to β is along the aperture. Equation 2.49 will only produce

a real angle of radiation if $\mid \beta \mid < k_0$, which denotes that leaky-wave radiation can only occur when waves are moving fast along the waveguide [23]. Waves with a lower frequency and moving slower than the speed of light will produce bounded waves while higher frequency waves will bring out leaky waves.

2.5.3 Beam Steering

The leaky wave transverse number has a relation to the angle of its region, the propagation constant of the surface wave, the surface impedance, and the impedance period, seen in Eq. 2.45, Eq. 2.47 and Eq. 2.49 [24]. Ultimately this relation can be simplified to

$$k \sin \theta_0 \simeq \beta_{SW} - \frac{2\pi}{d}. \tag{2.50}$$

This relationship allows us to change the angle of the leaky wave's main beam. Because the wavelength is also related to the wave number, a change in the period can also play a part in a backward (d $< \lambda_{SW}$) or forward (d $> \lambda_{SW}$) beam. A backward beam will correspond to a negative θ_0 value and a positive θ_0 represents a forward wave. When the period is equal to the surface wavelength, the beam will have $\theta_0 = 0$, or 'broadside'.

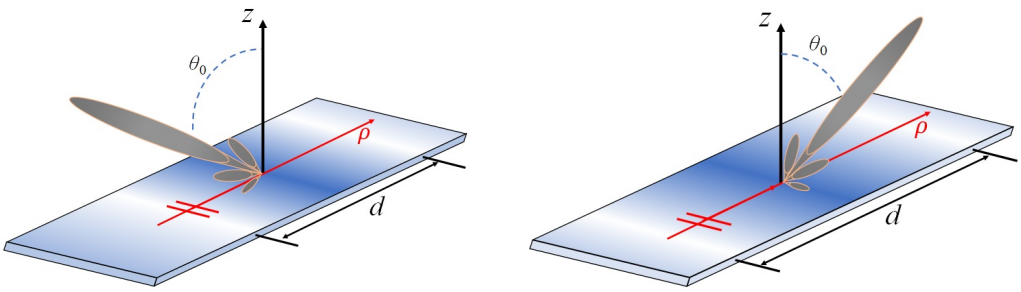

(a) Smaller value of d, resulting in backwards wave.

(b) Larger value of d, resulting in forward wave.

Figure 2.17: The direction a leaky wave is directed can be a result of its period, d due to the relation between wavelength and wave number. A period less than the wavelength, $d < \lambda_{SW}$ will result in a backward wave. Conversely, if the period is greater than the wavelength, $d > \lambda_{SW}$, the leaky wave will be directed forward.

CHAPTER 3: DESIGN AND ANALYSIS

This chapter discusses the process for developing a reconfigurable modulated metasurface aperture antenna. The premise of this antenna consists of a metasurface with periodically modulated patches that turn a non-radiating mode into a radiating leaky mode. A simulation program that implements Periodic Green's Function and the method of moments is used to determine the behaviors of the models by finding the scattering and wave parameters. The formation of the modulated surface is explained, starting with the unit cell and assumptions. The unit cell is then used to develop a periodic structure that will undergo simulation in the far field. These results will be analyzed and compared against various iterations of the structure. To show the versatility of the design, a metasurface designed at a vastly different frequency will then be assembled and simulated to show that both surfaces radiate effectively and comparably.

3.1 Design

Leaky wave antennas can be classified as uniform, quasi-uniform, or periodic; in one or two dimensions. The chosen design consists of a one-dimensional, periodic antenna. The following section describes the process and steps used to design and configure the modulated surface for the reconfigurable metasurface antenna.

3.1.1 Unit Cell

Local periodicity is assumed because the size of the unit cell is much smaller than the wavelength. Variations of the unit cell are examined and used to create the surface with modulated impedance. The basic geometry of the unit cell is made up of rectangular PEC unit cells with an aperture in the center. The PEC patch is placed

at a designated height, h, above a ground plane and is separated by air. The length of the aperture, L_x, varies amongst adjacent unit cells while the aperture width, L_y, and unit cell parameters P_x (length) and P_y (width) stay constant. The initial value of h is chosen to allow enough room for the actuators, as well as setting the parameters to ensure broadside design with no change. A table of these variables and values can be seen in Table 3.1.

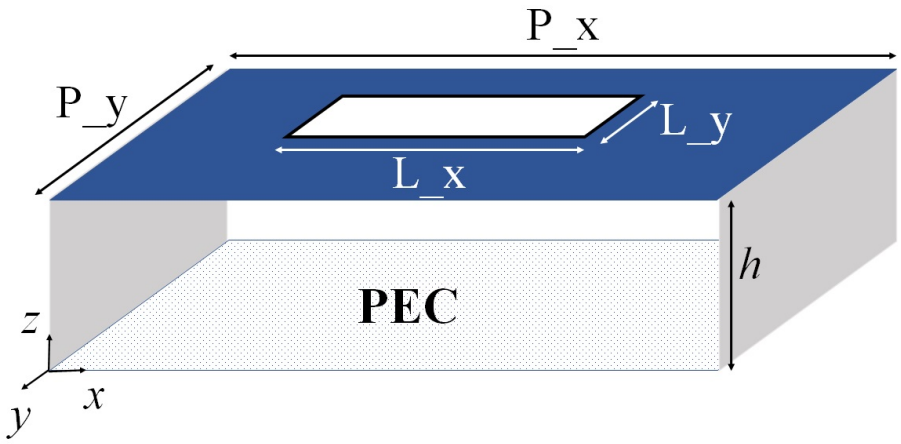

Figure 3.1: Representation of the unit cell of the metasurface. Consists of a top PEC sheet with an aperture located in the middle of it. The PEC has dimensions P_x and P_y and aperture dimensions L_x and L_y. The bottom sheet is a ground plane and is separated by air at distance, h.

Table 3.1: Unit Cell Parameter Values for 183 GHz

Parameter	**Measurement (μm)**
λ	1638
P_x	590
P_y	180
L_x	250
L_y	110
h	38

The initial length of the unit cell is chosen to satisfy local periodicity and also

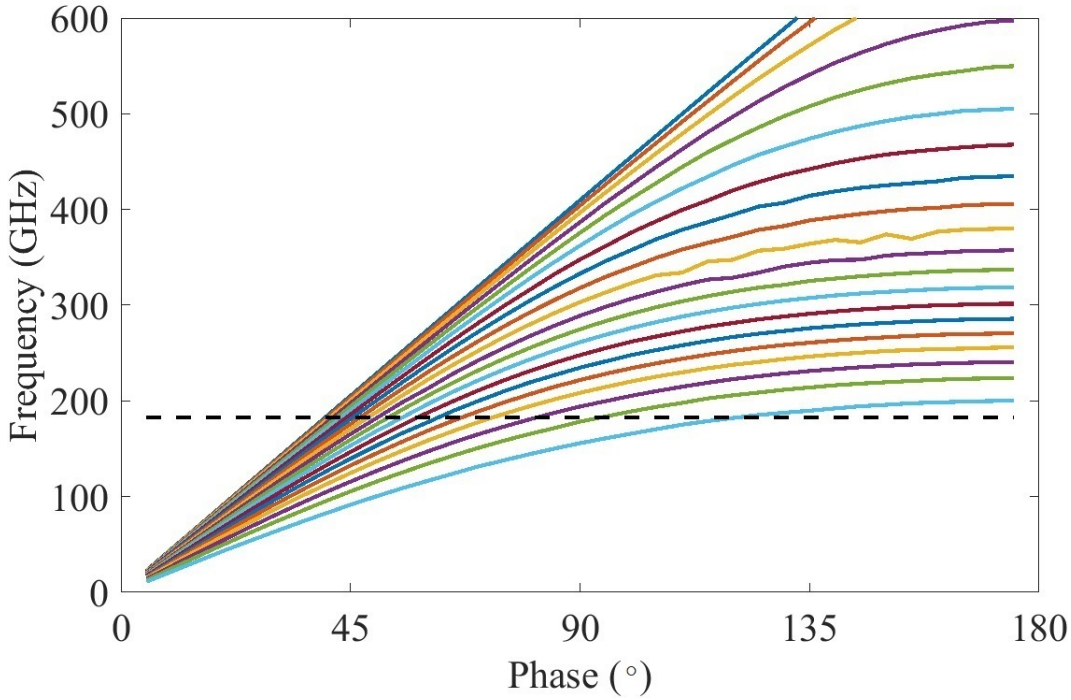

Figure 3.2: A dispersion curve representing the phase in degrees of different length apertures against its corresponding frequency (GHz). The designed frequency of 183 GHz is represented by a black dashed line and shows where data is further extrapolated from.

provide enough variation in impedance values. The unit cell needs to have a large range to match the theoretical impedance modulation required on the surface in order to propagate in the designated directions. At 183 GHz, the aperture lengths range from 100 μm to 590 μm and a database is created based on the eigenmodes related to each aperture length. The dispersion curves gathered from each aperture size is gathered and shown in Fig. 3.2 where each curve represents a different size and the black, dashed line is the design frequency, 183 GHz. The phase is gathered at the intersection of the design frequency for every height. That phase is converted to radians and divided by the period of the unit cell in order to find the wave number for each size. Using Eq. 2.47, all of the impedance values can be found for each of the different sizes at the design frequency.

To make a complete database, the remaining values are found through interpola-

tion. As shown in Fig. 3.3, the purple circles show the impedance values extrapolated from the dispersion data, and the solid, blue line shows the full impedance database for a range of aperture lengths.

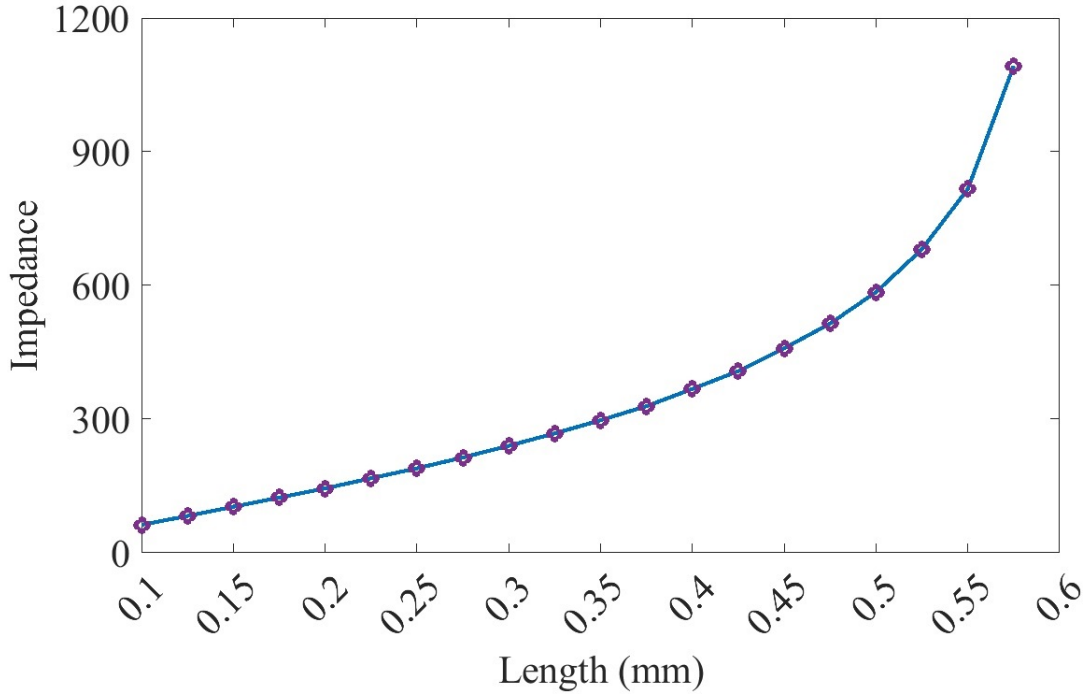

Figure 3.3: Expanded database of aperture lengths with corresponding impedance values at 183 GHz. The data extrapolated from the unit cell dispersion curve are represented with dots and the interpolated values are represented along the curved line.

3.1.2 Periodic Structures

By implementing local periodicity assumption and using the constructed database, the different aperture lengths are used to construct the modulated surface. The modulation period of this surface is determined using the Eq. 2.50. This equation relates the wave number to the angle of the main beam of the leaky wave. Since the frequency is fixed at 183 GHz, the modulation is adjusted to steer the beam broadside, which means θ_0 is equal to zero.

The impedance database is used to match the theoretical surface impedance in order to design the metasurface. The modulation period of the unit cell, d, determines

how many unit cells are in each modulation period. A generalized diagram of this period structure can be seen in Fig. 3.4 relating the aperture length to a corresponding impedance value. Each unit cell with a different impedance value and aperture length can be distinguished through the blue gradient. The generated metasurface has ten impedance modulation periods of this structure repeated along the y direction. To avoid impedance mismatches, eight cells that have no aperture are added on each side connecting to each end port. The configuration of modulation periods and blank cells is designed to maximize directivity. The length ensures that most of the energy has radiated up by the end of the antenna to avoid reflections.

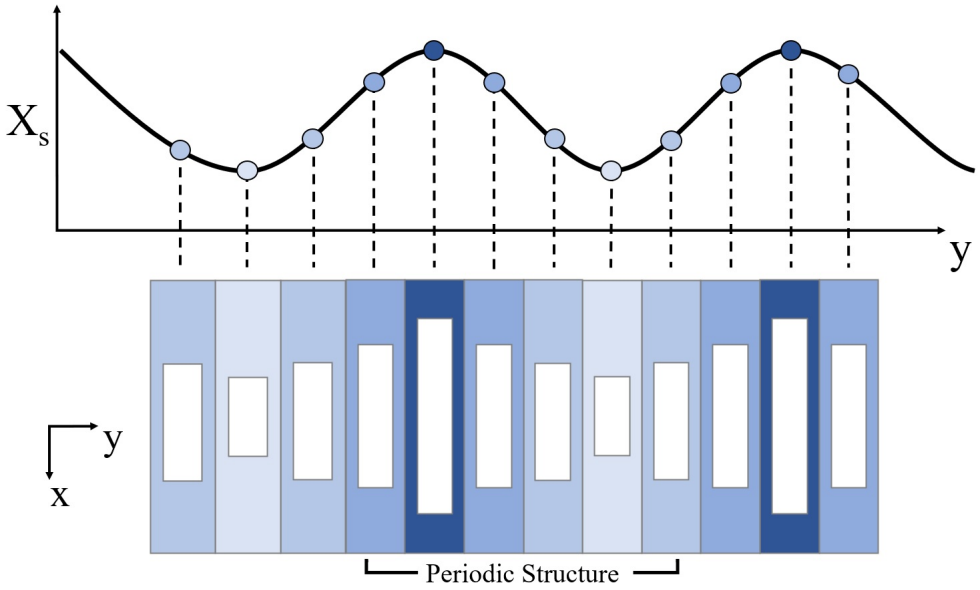

Figure 3.4: Visualization of a modulated surface with a periodic structure. Each unit cell with a different impedance value and aperture length can be distinguished through the gradient of color. The unit cells are arranged sinusoidally based on their corresponding impedance values.

3.1.3 Configuration

The prototype for the reconfigurable modulated aperture antenna consists of two piezoelectric actuators attached to the modulated metasurface and a ground plane of equal dimensions. These actuators are able to convert electrical energy directly into linear motion with high speed, force, precision, and virtually unlimited resolu-

tion. They are used currently in every modern high-tech field from semiconductor testing and inspection to super-resolution microscopy, bio-nanotechnology, and astronomy/aerospace technology [25]. Since the parameters in Eq. 2.47 are fixed, the antenna uses various distances between the metasurface and the ground plane to change the average impedance. The motion of the actuators adjusts the distance to meet the specified impedance. As stated earlier, and determined from Eq. 2.7, the impedance changes the wave number, ultimately allowing a change in the direction of the main beam.

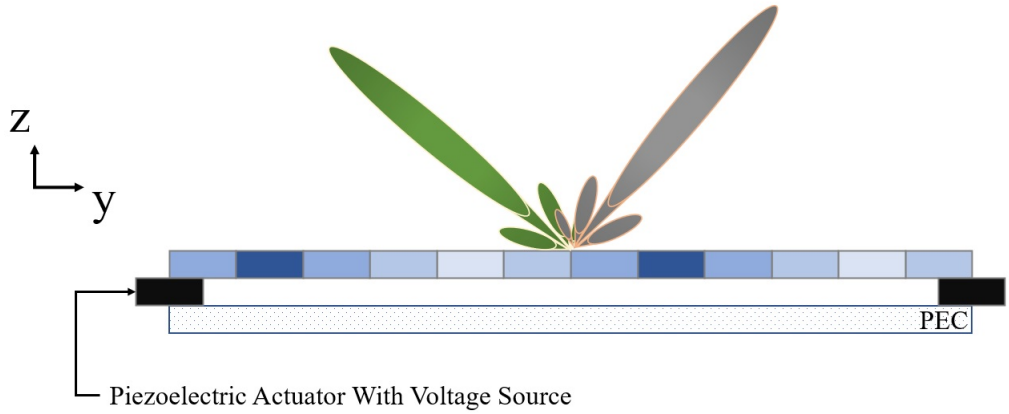

Figure 3.5: Theorized prototype of reconfigurable modulated aperture antenna consisting of the designed modulated metasurface attached to a ground plane by two piezoelectric actuators. The actuators change the distance between the metasurface and the ground plane based on the amount of voltage being applied to the actuator, ultimately allowing the antenna to change the direction of the beam.

3.2 Simulations and Results

This section discusses the various simulations conducted on the metasurface in the far field and the corresponding radiation patterns will be compared. The variations will include a height sweep, a material change, fabrication tolerances, and different port structure designs. The metasurface will then undergo the same design process at a different frequency to compare results.

The modulated surface undergoes simulation that uses Periodic Green's Function

and method of moments calculations to analyze the behavior of the surface to predict the antenna's directivity and gain. The antenna's fair field is set using an infinite sphere defined within the regions ϕ from -180° to 180° and θ at -90° to 90°. A portion of the simulated surface can be seen in Fig. 3.6 noting the PEC patches at the start of the metasurface along with a periodic arrangement of apertures.

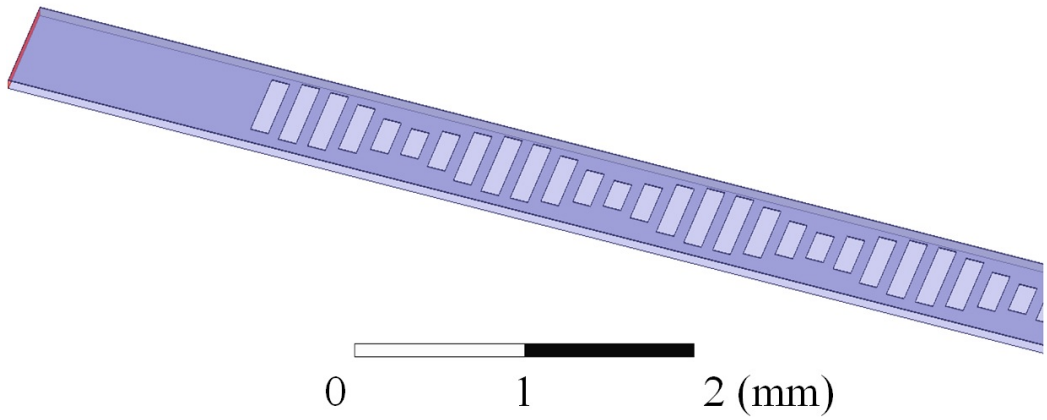

Figure 3.6: Model of modulated surface generated in HFSS. Apertures are arranged periodically as described in the previous sections along with PEC patches at the beginning of the metasurface.

3.2.1 Height Sweep

A height sweep is conducted on the metasurface from 0 μm to 700 μm, to show Δh and the nominal value of 38 μm corresponds to 0 μm. The results show that the initial metasurface design is successful for being designed at broadside, meaning $\theta = 0°$. The results from the height sweep reinforce the theoretical values derived from Eq. 2.47 and Eq. 2.50, deriving the leaky wave angles. The simulation results also reinforced the ability of the antenna's ability to beam steer through Δh. The resulting directivity plots can be referenced with a sample of Δh at 0 μm, 200 μm, 500 μm and 700 μm in Fig. 3.7. A corresponding table showing the values of the angles and dB can also be referred to in Table 3.2.

To ensure the precision of the simulated results, an angle predictor was created using various equations and the eigenmodes of the initial unit cell. The angle predictor

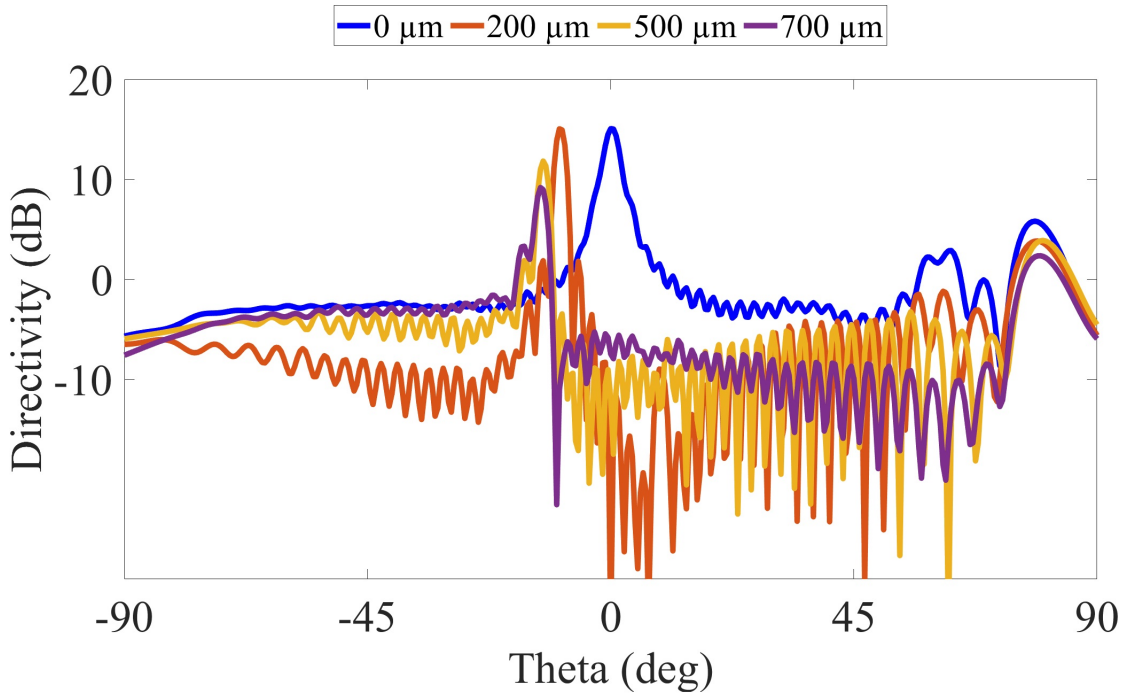

Figure 3.7: A directivity plot for the metasurface at 183 GHz at four Δh. The radiation pattern shows a strong correlation between the angle of the main beam and the distance between the MTS and the ground plane.

Table 3.2: Beam angles and corresponding directivity at Δh, for 183 GHz antenna.

Δh (μm)	**Angle**	**Directivity** (dB)
0	0.0°	15.1
200	-9.0°	15.1
500	-12.5°	11.8
700	-13.0°	9.2

uses the unit cell and generates two surfaces with modulated impedances. The first surface that is used uses the same procedure of creating a modulated surface at h, with a specific impedance found from the database and the dispersion curves. The second surface implements the variation of aperture lengths at Δh and creates a modulated surface with a new average impedance using the values from a new database and dispersion curves specific to that distance. The resulting angles of the two surfaces are compared to predict the distance between the surfaces and the ground plane. The predicted angles and the simulated angles showed little variation but had a 10.5% difference overall. The comparison can be referenced in Table 3.3.

Table 3.3: Predicted angles for the 183 GHz antenna at Δh.

Δh (μm)	**Predicted**	**Simulated**
0	-0.1°	0.0°
100	-6.7°	-6.5°
200	-9.3°	-9.0°
300	-10.6°	-10.5°
400	-11.3°	-11.5°
500	-11.7°	-12.5°
600	-12.0°	-13.0°
700	-12.2°	-13.0°

3.2.2 Aluminum Design

The initial simulated model uses the theoretical characteristics of a PEC as the material for the modulated surface. Ultimately, to fabricate this design for real-world applications it would need to be constructed out of real material. A PEC is a perfect conductor of electricity, these characteristics result in infinite relative permittivity and being lossless. A PEC conducts electricity infinitely, having zero resistance. Among the most common materials used for electrical conductors, aluminum alloy (A96061) has the lowest electrical resistivity of 3.99 $\times$ 10^{-6} Ω/cm [26], making it an ideal candidate to use for fabrication.

Simulations using aluminum alloy in the described design are conducted in the same manner as the PEC. At the sample heights, aluminum alloy showed extremely comparable results, the angles showed a 1.4% difference and the directivity 1.07%. Based on this difference and the properties that aluminum alloy possesses, it proves to be a viable option used for this design and fabrication.The resulting directivity plots for Δh can be seen in Fig. 3.8 with corresponding values in Table 3.4.

3.2.3 Fabrication Tolerances

One of the possible issues with a metasurface designed at the microscopic level is variance due to fabrication. A slight change in a design can cause the overall product differ from the design specifications, malfunction, measure incorrectly or

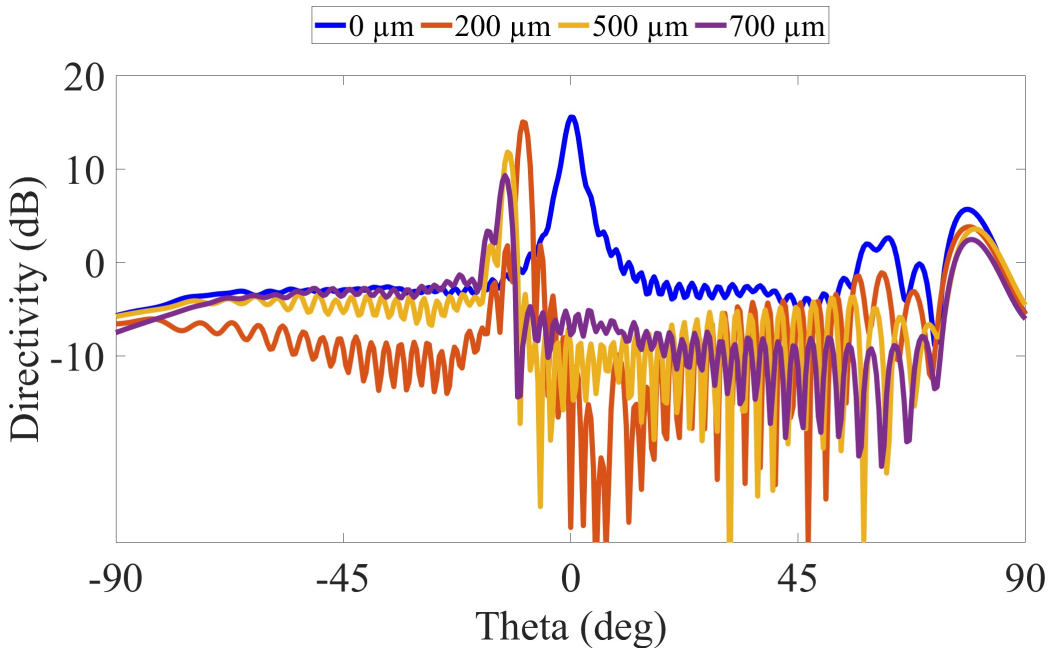

Figure 3.8: A directivity plot for the aluminum alloy antenna at 183 GHz. The four Δh can be noted by the different colors. The corresponding radiation pattern still shows the same correlation as the PEC, in terms of directivity and corresponding angles.

Table 3.4: Beam angles and corresponding directivity at Δh for the aluminum alloy antenna at 183 GHz.

Δh (μm)	**Angle**	**Directivity** (dB)
0	0.0°	15.5
200	-9.5°	15.0
500	-12.5°	11.8
700	-13.0°	9.3

even be dangerous and cause harm. To reenact the possibility of these flaws or errors during fabrication, tolerance metasurfaces are developed. They are studied using the unit cell, the local code, a tolerance percentage, and a random number generator. The surfaces are generated in a similar manner using the unit cell and creating a modular surface with apertures of different lengths. The random number generator is used with the tolerance percentage to create possible variations in the aperture lengths. To double down on possible fabrication errors, these imperfect surfaces were simulated using aluminum alloy. By developing these distorted metasurfaces,

a prediction of how accurately and efficiently the antenna will radiate can be noted based on the imperfections. The accumulation of the tolerance antennas showed a 0.375% difference when comparing the angles of the main beam and a 0.48% in terms of directivity. The directivity plots of the original surface and the distorted tolerance antennas can be referred to in Fig. 3.9 and Table 3.5.

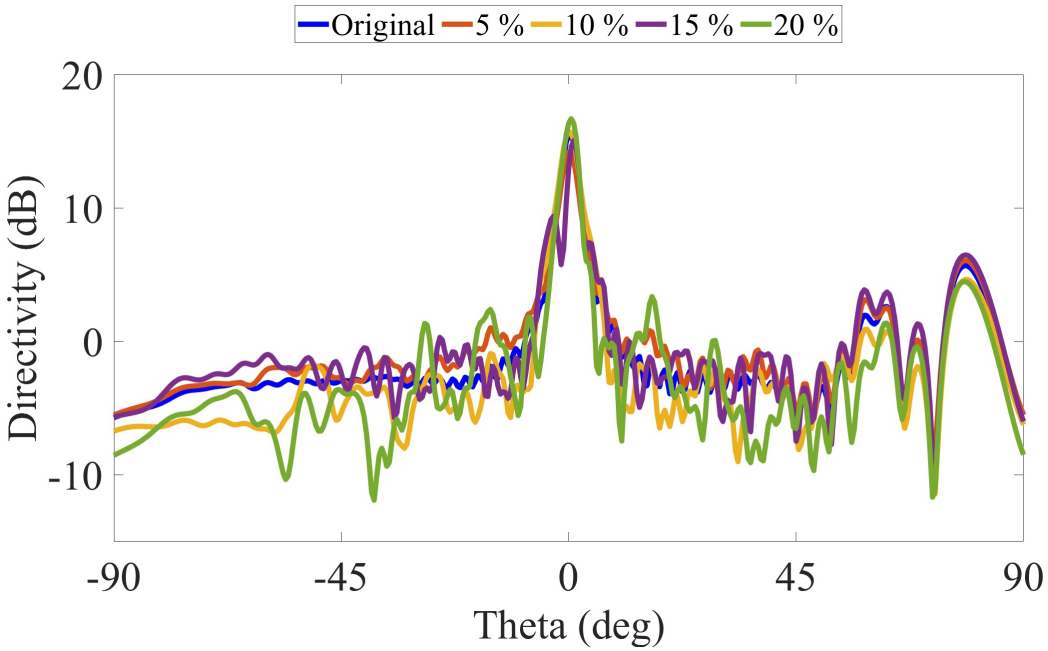

Figure 3.9: Directivity plots comparing metasurfaces made out of aluminum alloy with possible defects to due fabrication errors. The variation of error is simulated to show the deviation from the original design.

Table 3.5: Beam angles and directivity of tolerance antennas for 183 GHz.

Tolerance	**Angle**	**Directivity** (dB)
Original	0.0°	15.5
5%	0.0°	14.2
10%	0.0°	15.7
15%	1.0°	15.1
20%	0.5°	16.7

3.3 Design Changes

The radiation pattern shows a slight mismatch loss seen by the large side lobe near 80 degrees. The mismatch can be accredited to the difference between the source and

the surface impedance. To minimize the loss, the ends of the MTS were redesigned to change the average impedance. The first redesign, V2 (Fig.3.10b), consists of eight apertures of increasing length and impedance leading up to the start of the initial modulation design. This design will replace the solid sheet of material used during the initial simulations. Another design change, V3 (Fig.3.10c), added the same eight increasing apertures leading up to the start of the modulation design after the solid sheet of material. The variations can be seen compared to the initial design in Fig. 3.10. The start of the modulation on the surface is noted with an arrow.

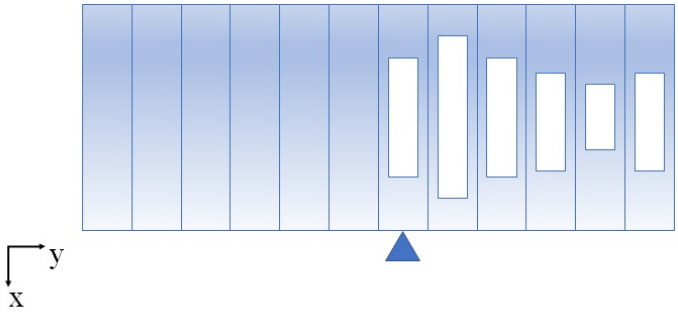

(a) Initial design consisting of eight blank unit cells leading up to the modulated surface.

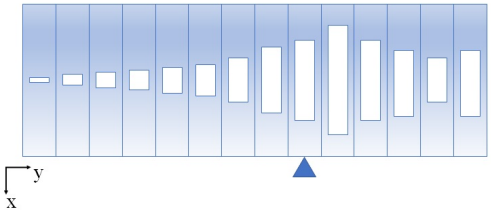

(b) V2, the first redesign that replaces the solid sheet of aluminum alloy with eight apertures of gradually increasing aperture length leading up to the first aperture length of the initial modulated surface.

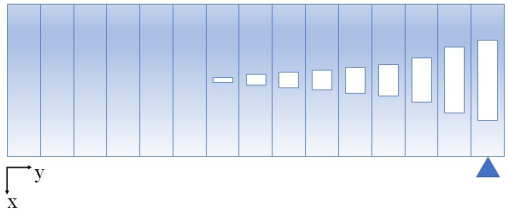

(c) V3, is the second redesign that implemented the eight gradually increasing unit cells from V2, after the original eight blank unit cells.

Figure 3.10: Modifications implemented to reduce the mismatch loss caused by the source and surface impedance. The modulation starts on all three versions noted by the arrow. All versions are simulated with aluminum alloy.

To have the most realistic results of the design change, the two variations were simulated using aluminum alloy. resulting in a sheet of aluminum alloy for design V3. The results of the modifications can be referenced in Fig. 3.11, comparing them to the initial design. The modifications showed minimal variance in directivity. Similarly, there were no significant changes in the side lobe after the attempt to match the impedances, so other designs are currently being configured for optimization. The slight variations did provide insight to that the average impedance values were affecting the mismatch and sidelobes.

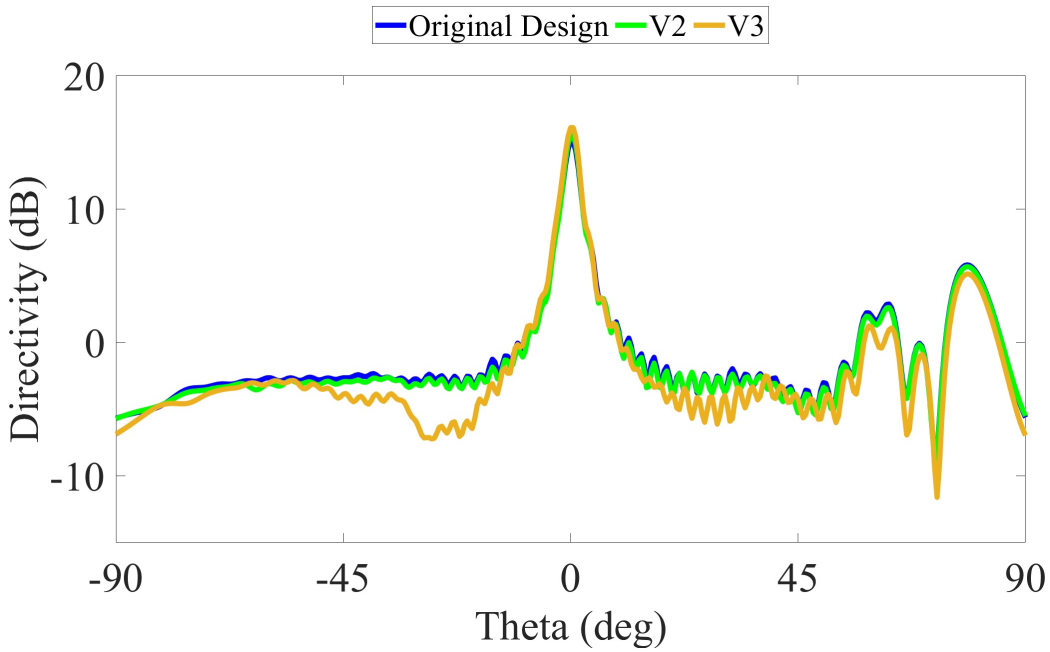

Figure 3.11: Directivity plots comparing redesigned metasurface ends, all variations can be seen in Fig. 3.10. The redesign is implemented to combat mismatch losses from the source and the surface impedance of the MTS by adding gradual apertures to the start of the surface modulation in different instances. The modifications showed little variance, so other designs are currently being configured for optimization.

3.4 Frequency Reconfiguration

To illustrate the versatility of the design, a second antenna is configured to operate at 325 GHz using the same methods. The inversely proportional relationship between frequency and wavelength resulted in an antenna nearly half the size of the first due to

the doubling frequency. Being able to adjust the operating frequency of the antenna can be used to meet the exact demands of various applications relating to long-distance communications, navigation, radar, or wherever need be. The change in frequency can provide insight into how the frequency will affect the overall antenna in terms of geometric size, efficiency, and usability. The unit cell and antenna will feature the same configuration of the metasurface atop a ground plane, separated by distance, h. The parameters used for this new unit cell can be seen in Table 3.6.

Table 3.6: Unit Cell Parameter Values for 325 GHz

Parameter	**Measurement (μm)**
λ	922
P_x	330
P_y	110
L_x	150
L_y	60
h	20

The range for the aperture lengths is also smaller, ranging from 50 μm to 300 μm. The unit cell is simulated in the same sense as the initial unit cell to generate the eigenmodes for the various aperture lengths. A dispersion curve of these apertures is generated and used to determine the phase and frequency of the different-sized apertures at the new operating frequency. The dispersion curve can be seen in Fig. 3.12, where the different aperture lengths are distinguished with various colors and the frequency, 325 GHz, is noted with the dashed black line.

Using the information from the dispersion curve, a second database is created for the new frequency, comparing aperture lengths to their relative impedances. These values are used to determine more specific impedances through interpolation. The simulated values are plotted and a curve is used to estimate the impedance values

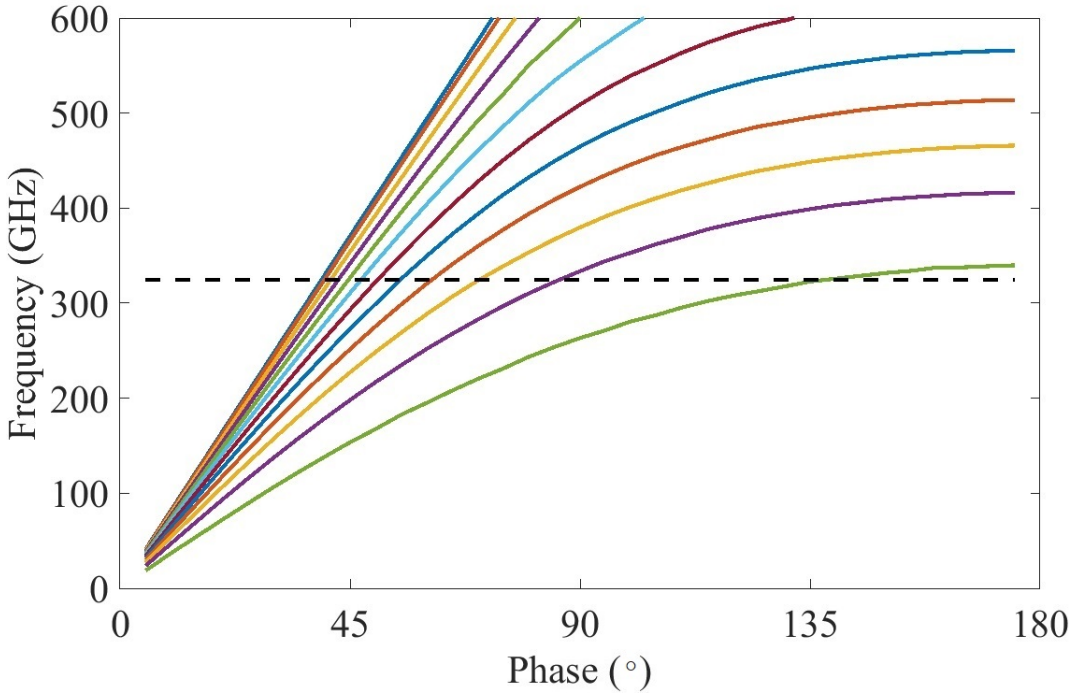

Figure 3.12: A dispersion curve created from the 325 GHz unit cell. The aperture lengths were plotted by comparing their respective phase, in degrees, to the frequency (GHz). 325 GHz is represented by a black dashed line and shows where data is further extrapolated from.

for the in-between aperture lengths. This information can be referenced in Fig. 3.13, with the simulated data represented by points and the interpolated data along the curve.

From this database, apertures are chosen based on their impedances to create a modular surface. The surface included ten periodic arrangements and blank patches on each end to meet the determined average surface impedance and be modular. This surface is simulated at various values of Δh, ranging from 0 μm to 350 μm, to determine the phase angle and directivity. Compared to the 183 GHz antenna, the angle of the main beam had a 0.13% difference and a 4.5% difference in directivity. The 325 GHz surface followed the same suit as the initial one in terms of beam steering and directivity. The resulting directivity plots can be referenced in Fig. 3.14, and the corresponding angles and directivity can be read in Table 3.7.

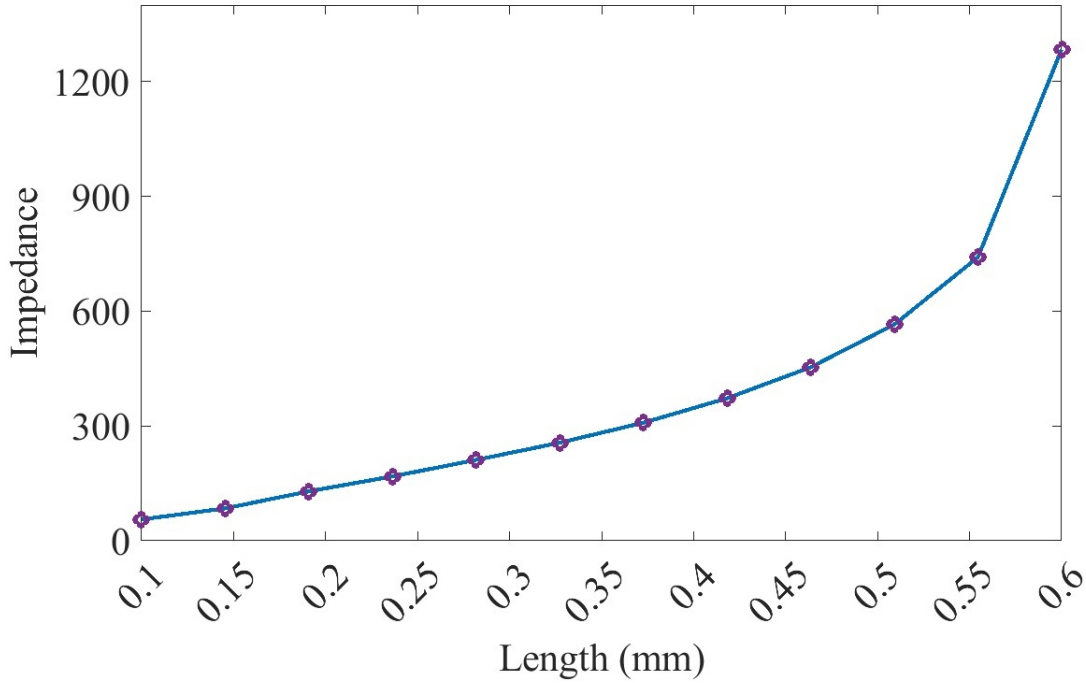

Figure 3.13: Interpolated impedance values for the aperture lengths of the 325 GHz unit cell. The simulated values are represented by points and the interpolated data can be seen along the curve.

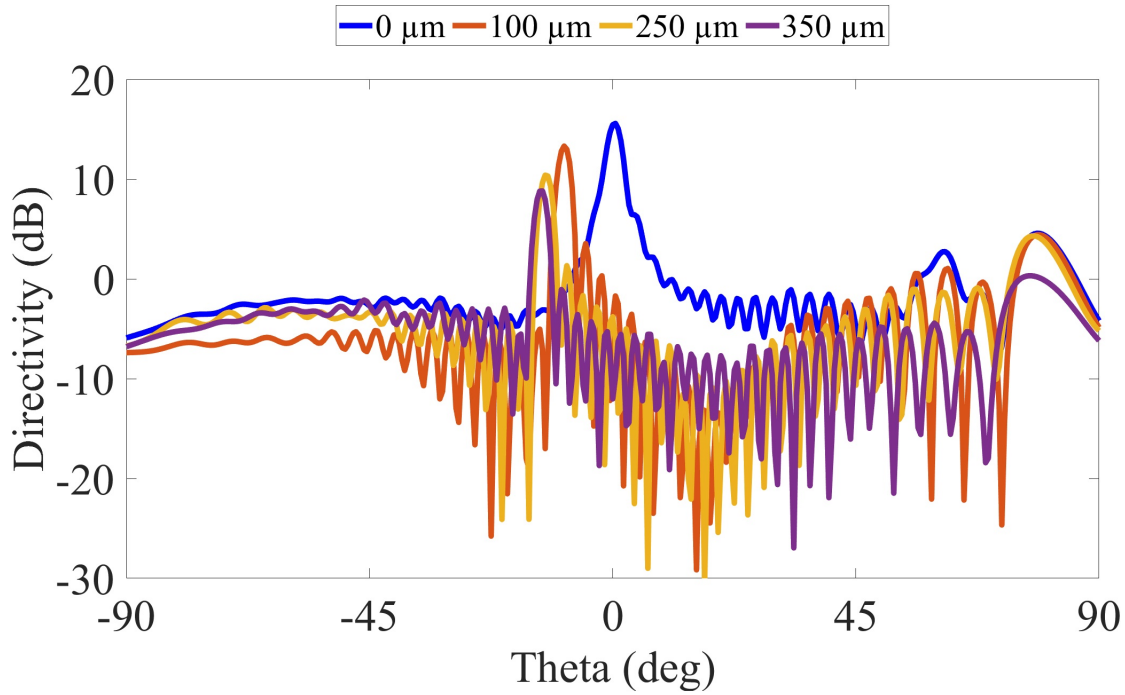

Figure 3.14: Directivity plots for Δh for the 325 GHz antenna. The plot reveals the same correlation as the 183 GHz in terms of angle and height change, for a smaller height range.

Table 3.7: Beam angles and corresponding directivity at Δh for 325 GHz antenna.

Δh (μm)	**Angle**	**Directivity** (dB)
0	-0.5°	15.6
100	-9.0°	13.3
250	-12.5°	10.4
350	-13.0°	8.8

The angle predictor is modified for 325 GHz. The angle predictor used the same format of using a unit cell and creating two surfaces with different impedances and using them to predict the angles and heights from equations relating surface impedance and leaky waves. This angle predictor is used to verify the results of the simulation as well as compare the results of the previous angle predictor for the 183 GHz surface. The angle predictor showed a 10.9% difference between the predicted and simulated angles, which is comparable to the 10.5% of the 183 GHz surface. The results comparing the two are displayed in Table 3.8.

Table 3.8: Predicted angles for the 325 GHz antenna at Δh.

Δh (μm)	**Predicted**	**Simulated**
0	-0.1°	-0.5°
50	-6.3°	-6.0°
100	-9.0°	-9.0°
150	-10.3°	-10.5°
200	-11.1°	-11.5°
250	-11.6°	-12.5°
300	-11.9°	-12.5°
350	-12.1°	-13.0°

To simulate the capabilities of this antenna for manufacturing, the surface is simulated using aluminum alloy. This material proved earlier to have comparable characteristics of a PEC. The angles of the aluminum surface differed from the PEC by 1%, and the directivity by 2.6%, both are showing promising results. The results of the aluminum alloy surface can be referenced in Fig. 3.15 and Table 3.7.

While the values of the aluminum alloy surface provided promising results, surface variation due to fabrication is still possible. The surface, designed in the order of

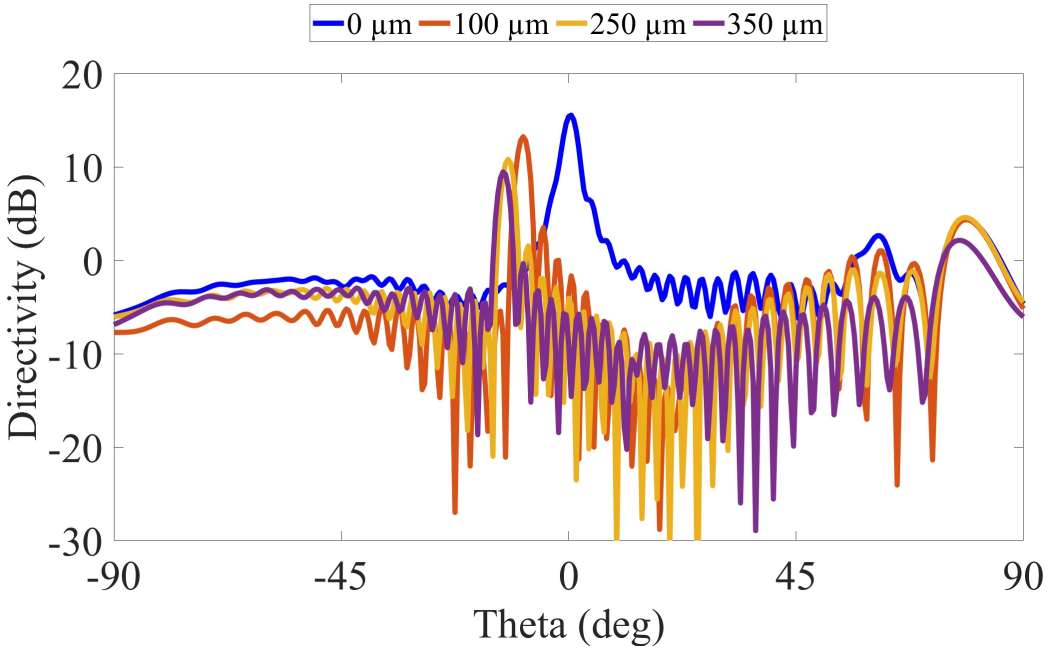

Figure 3.15: Directivity plots at Δh for the aluminum alloy 325 GHz metasurface. Different colors represent the Δh. The Δh shows the same correlation to the beam angle as the previous metasurface.

Table 3.9: Beam angles and corresponding directivity at Δh for the aluminum alloy antenna at 325 GHz

Δh (μm)	**Angle**	**Directivity** (dB)
0	0.5°	15.5
100	-9.0°	13.2
250	-12.0°	10.8
350	-13.0°	9.5

microns, would need precision printing to meet the exact dimensions. Tolerance antennas are created at this frequency to determine how distorted the antennas could be manufactured and still be safe to use for applications. The result of the tolerance antennas compared to the original antenna at the nominal height can be referred to in Fig. 3.16 and Table 3.10.

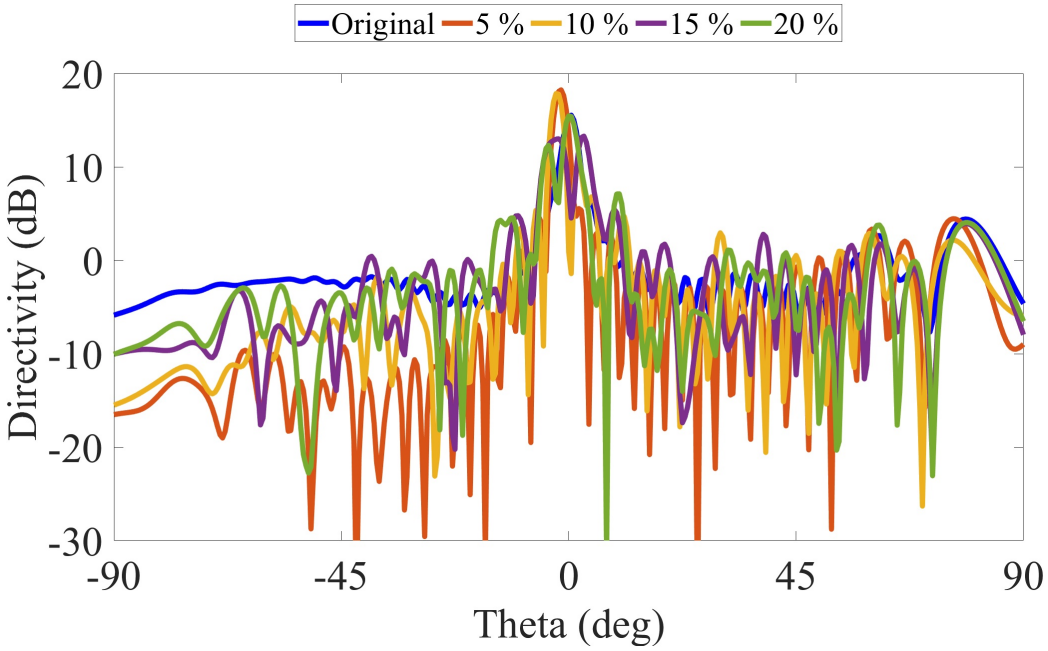

Figure 3.16: Directivity plots comparing metasurfaces made out of aluminum alloy with possible defects due to fabrication errors at 325 GHz. The error variation is simulated to show the deviation from the original design.

Table 3.10: Beam angles and directivity of tolerance antennas for 325 GHz.

Tolerance	**Angle**	**Directivity** (dB)
Original	0.0°	15.5
5 %	-1.5°	18.2
10 %	-2.5°	17.8
15 %	3.0°	13.3
20 %	0.0°	15.5

The results of the antenna designed for 325 GHz showed very similar results to the 183 GHz antenna. The most significant finding was the dimensions of the unit cell and antenna, which was expected due to the proportional relationship between frequency

and wavelength. The change of frequencies did not significantly affect the antenna's performance, which suggests that design is more important than the frequency for achieving optimal results and providing the design's versatility.

CHAPTER 4: CONCLUSION

This thesis presented a reconfigurable leaky wave antenna prototype with a tunable impedance surface for radio frequency applications. The design parameters were based on the operating frequency of 183 GHz. The antenna was constructed from a singular aperture surface unit cell atop a ground plane separated by a distance, h. The unit cell was analyzed with different-sized apertures to create a database relating the aperture sizes to their impedance value. This database provided the specific parameters to create a periodic structure used for the antenna's full-length modular surface.

Simulations of the modular surface were conducted at varying heights to promote a change in surface impedance. To verify the initial results of the simulation, an angle predictor was created using various formulas relating to leaky waves. The simulation results showed the correlation between changes in distance, impedance, and angle and considerable results with the angle predictor. To encourage the fabrication of the antenna, the surface was simulated using aluminum alloy and tested for possible fabrications utilizing a range of potential error tolerances. The versatility of the design was proven by designing a similar surface operating at 325 GHz. This surface followed the same simulations with nearly identical results.

The prototype of the antenna consists of the modular surface and a ground strip of equal dimensions. The surface and ground strip are connected by two piezoelectric actuators that can reconfigure the distance between the two in a one-dimensional motion. The distance change between the surface and the ground patch changes the antenna's impedance, ultimately changing the direction of the main beam.

The results of the prototype for the reconfigurable metasurface antenna accomplished the overall goals of a tunable surface, reconfigurability, and beam steering

with the use of actuators. It can be designed and utilized in various research fields and has potential applications in multiple areas, such as optics, antennas, and electronics. The low profile, low cost, and high efficiency make it a highly sought alternative to traditional bulkier and heavier antennas for satellites, radars, or any application with electromagnetic devices.

As research into metasurfaces progresses, this antenna can be used for further development in studying metasurfaces and other novel structures. Metasurfaces have the potential to revolutionize the way we interact with light, sound, and other forms of energy, and the potential for new and exciting applications is limitless.

REFERENCES

[1] D. R. Smith, W. J. Padilla, D. C. Vier, S. C. Nemat-Nasser, and S. Schultz, "Composite medium with simultaneously negative permeability and permittivity," *Phys. Rev. Lett.*, vol. 84, pp. 4184–4187, May 2000.

[2] M. Faenzi, G. Minatti, D. Gonzalez-Ovejero, F. Caminita, E. Martini, C. D. Giovampaola, and S. Maci, "Metasurface antennas: New models, applications and realizations," *Scientific Reports*, vol. 9, 2019.

[3] T. Li and Z. N. Chen, "A dual-band metasurface antenna using characteristic mode analysis," *IEEE Transactions on Antennas and Propagation*, vol. 66, no. 10, pp. 5620–5624, 2018.

[4] H. Wang, Y. Li, H. Chen, Y. Han, S. Sui, Y. Fan, Z. Yang, J. Wang, J. Zhang, S. Qu, and Q. Cheng, "Multi-beam metasurface antenna by combining phase gradients and coding sequences," *IEEE Access*, vol. 7, pp. 62087–62094, 2019.

[5] C. A. Balanis, *Antenna Theory: Analysis and Design.* Wiley-Interscience, 4th ed., 2005.

[6] V. G. Veselago, "The electrodynamics of substances with simultaneously negative values of ε and μ," *Physics-Uspekhi*, vol. 10, no. 4, pp. 509–514, 1968.

[7] J. Pendry, "Negative refraction makes a perfect lens," *PHYSICAL REVIEW LETTERS*, vol. 85, pp. 3966–3969, 2000.

[8] G. Minatti, F. Caminita, E. Martini, M. Sabbadini, and S. Maci, "Synthesis of modulated-metasurface antennas with amplitude, phase, and polarization control," *IEEE Transactions on Antennas and Propagation*, vol. 64, no. 9, pp. 3907–3919, 2016.

[9] M. Boyarsky, T. Sleasman, L. Pulido-Mancera, T. Fromenteze, A. Pedross-Engel, C. M. Watts, M. F. Imani, M. S. Reynolds, and D. R. Smith, "Synthetic aperture radar with dynamic metasurface antennas: a conceptual development," *JOSA A*, vol. 34, no. 5, pp. A22–A36, 2017.

[10] Y. Braham Chaouche, M. Nedil, M. Olaimat, M. El Badawe, and O. M. Ramahi, "Wearable metasurface antenna based on electrically-small ring resonators for wban applications," *Electronics Letters*, vol. 58, no. 1, pp. 4–7, 2022.

[11] N. Ida, *Engineering Electromagnetics.* Springer Publishing Company, Incorporated, 2nd ed., 2007.

[12] A. Mohsen, "On the impedance boundary condition," *Applied Mathematical Modelling*, vol. 6, no. 5, pp. 405 – 407, 1982.

[13] T. B. A. Senior, "Impedance boundary conditions for imperfectly conducting surfaces," *Springer Nature*, Jan. 1960.

[14] C. H. Papas, *Theory of electromagnetic wave propagation*. Dover Publications Inc., 1965.

[15] N. Engheta and R. Ziolkowski, *Metamaterials: Physics and Engineering Explorations*. John Wiley and Sons, Sept. 2006.

[16] John L. Volakis, Arthur A Oliner, and David R. Jackson, *Antenna Engineering Handbook*. McGraw-Hill Education, 2007.

[17] Constantine A. Balanis, ed., *Modern Antenna Handbook*. Wiley-Interscience, 1st ed., Sept. 2011.

[18] J. KÃ€stel and M. Fleischhauer, "Quantum electrodynamics in media with negative refraction," *Laser Physics*, vol. 15, 01 2005.

[19] C. L. Holloway, E. F. Kuester, J. A. Gordon, J. O'Hara, J. Booth, and D. R. Smith, "An overview of the theory and applications of metasurfaces: The two-dimensional equivalents of metamaterials," *IEEE Antennas and Propagation Magazine*, vol. 54, no. 2, pp. 10–35, 2012.

[20] M. A. Francavilla, E. Martini, S. Maci, and G. Vecchi, "On the numerical simulation of metasurfaces with impedance boundary condition integral equations," *IEEE Transactions on Antennas and Propagation*, vol. 65, 2015.

[21] A. Oliner and A. Hessel, "Guided waves on sinusoidally-modulated reactance surfaces," *IRE Transactions on Antennas and Propagation*, vol. 7, no. 5, pp. 201–208, 1959.

[22] F. Monticone and A. Alu, "Leaky-wave theory, techniques, and applications: From microwaves to visible frequencies," *Proceedings of the IEEE*, vol. 103, no. 5, pp. 793–821, 2015.

[23] A. Oliner, "Leaky waves: basic properties and applications," in *Proceedings of 1997 Asia-Pacific Microwave Conference*, vol. 1, pp. 397–400 vol.1, 1997.

[24] M. Mohsen, M. S. Mohamad Isa, M. Isa, M. S. I. Mohd Zin, S. Saat, Z. Zakaria, I. Ibrahim, M. Abu, A. Ahmad, and M. Abdulhameed, "The fundamental of leaky wave antenna," *Journal of Telecommunication, Electronic and Computer Engineering*, vol. 10, pp. 119–127, 01 2018.

[25] P. USA, "Piezoelectric actuators."

[26] A. Inc, "Asm material data sheet."

APPENDIX A: Introduction Figures

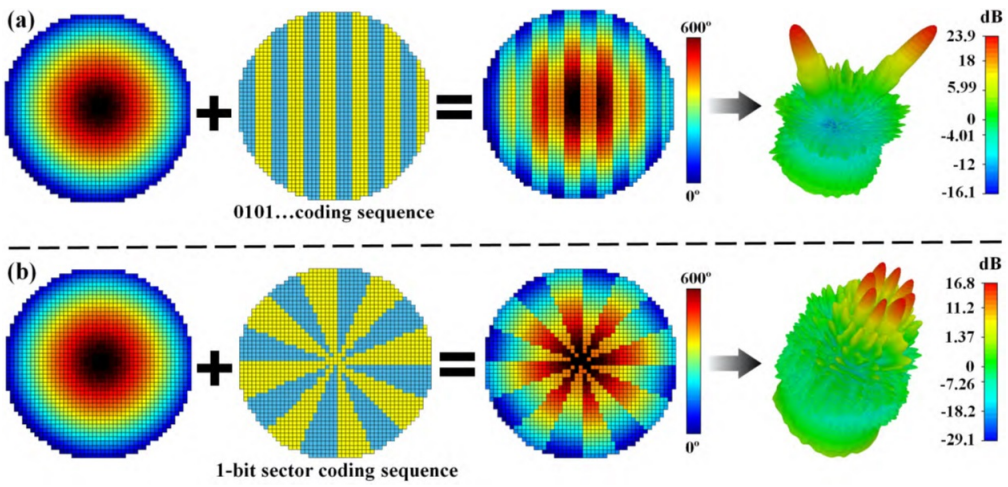

Figure A.1: Phase distribution and simulated far-field radiation pattern of (a) double-beam metasurface reflector antenna, (b) eight-beam metasurface reflector antenna [4].

(a) (b) (c)

Figure A.2: The other examples of textures used for implementing the MTS: (a) patch with slot, (b) patch with cross slot and (c) double π [2].